The Astronomical Journal, 164:126 (20pp), 2022 October https://doi.org/10.3847/1538-3881/ac8357

White Dwarf Binaries across the H-R Diagram

Borja Anguiano[1], Steven R. Majewski[1], Keivan G. Stassun[2], Carles Badenes[3], Christine Mazzola Daher[3], Don Dixon[2], Carlos Allende Prieto[4,5], Donald P. Schneider[6], Adrian M. Price-Whelan[7], and Rachael L. Beaton[8]
[1] Department of Astronomy, University of Virginia, Charlottesville, VA 22904, USA; astrobaj@gmail.com
[2] Department of Physics & Astronomy, Vanderbilt University, 2301 Vanderbilt Place, Nashville, TN 37235, USA
[3] Department of Physics and Astronomy and Pittsburgh Particle Physics, Astrophysics and Cosmology Center (PITT PACC), University of Pittsburgh, 3941 O'Hara Street, Pittsburgh, PA 15260, USA
[4] Instituto de Astrofísica de Canarias, E-38205 La Laguna, Tenerife, Spain
[5] Universidad de La Laguna, Dpto. Astrofísica, E-38206 La Laguna, Tenerife, Spain
[6] Department of Astronomy & Astrophysics, Pennsylvania State University, University Park, PA 16802, USA
[7] Center for Computational Astrophysics, Flatiron Institute, 162 5th Avenue, New York, NY 10010, USA
[8] The Observatories of the Carnegie Institution for Science, 813 Santa Barbara Street, Pasadena, CA 91101, USA
Received 2022 May 17; revised 2022 July 12; accepted 2022 July 20; published 2022 September 6

Abstract

We created the APOGEE-GALEX-Gaia catalog to study white dwarf (WD) binaries. This database aims to create a minimally biased sample of WD binary systems identified from a combination of GALEX, Gaia, and APOGEE data to increase the number of WD binaries with orbital parameters and chemical compositions. We identify 3414 sources as WD binary candidates, with nondegenerate companions of spectral types between F and M, including main-sequence stars, main-sequence binaries, subgiants, sub-subgiants, red giants, and red clump stars. Among our findings are (a) a total of 1806 systems having inferred WD radii $R < 25\ R_{\oplus}$, which constitute a more reliable group of WD binary candidates within the main sample; (b) a difference in the metallicity distribution function between WD binary candidates and the control sample of most luminous giants ($M_H < -3.0$); (c) the existence of a population of sub-subgiants with WD companions; (d) evidence for shorter periods in binaries that contain WDs compared to those that do not, as shown by the cumulative distributions of APOGEE radial velocity shifts; (e) evidence for systemic orbital evolution in a sample of 252 WD binaries with orbital periods, based on differences in the period distribution between systems with red clump, main-sequence binary, and sub-subgiant companions and systems with main-sequence or red giant companions; and (f) evidence for chemical enrichment during common envelope (CE) evolution, shown by lower metallicities in wide WD binary candidates ($P > 100$ days) compared to post-CE ($P < 100$ days) WD binary candidates.

Unified Astronomy Thesaurus concepts: White dwarf stars (1799); Surveys (1671); Binary stars (154)

1. Introduction

The evolution of multiple-star systems is a fundamental question in stellar astrophysics. Most stars in these systems are widely separated (i.e., on long-period orbits), such that the pair does not interact strongly, and both stars evolve independently, as if single stars (Willems & Kolb 2004). However, around 25% of those are compact enough to exchange mass, changing the structures and subsequent evolution of both stars. For those systems with orbital periods less than ∼10 yr—"close" binaries—as the more massive component evolves from the main sequence (MS) to the red giant branch (RGB), the stars undergo a stage of common envelope (CE) evolution, where mass can be transferred to the lower-mass MS star and eventually leave behind a close, post-CE binary (PCEB) containing the core of the giant in the form of a white dwarf (WD) and its companion (e.g., Webbink 2008; Ivanova et al. 2013).

Physical understanding of CE evolution is extremely complicated from first principles, since there are too many length scales and timescales involved. Moreover, the CE phase is very short, 400–4000 yr (Hjellming & Taam 1991), and thus there are few known CE-phase candidates to provide observational constraints. For this reason, our primary strategy to understand the evolution of close binaries is to focus on the pre- and post-CE phases, and in particular on the obtention of systematic, unbiased, and statistically robust surveys of systems in those evolutionary stages. Subsequent stages of compact binary evolution are no less interesting, as they lead to a variety of phenomena that play significant roles in numerous areas of astrophysics, from the creation of a diverse taxonomy of variable stars to the production of sources of gravitational waves and cosmological standard candles. PCEBs are the progenitors of many interesting astrophysical transients observed across the electromagnetic spectrum, including cataclysmic variables (CVs), novae, Type Ia supernovae (SNe Ia), and some core-collapse SN subtypes (e.g., Toloza et al. 2019, and references therein). As a result, the properties of the binaries containing stellar remnants provide fundamental clues to understanding the varieties of subsequent evolution of PCEBs. However, the vast majority of these late evolutionary pathways start with a PCEB consisting of a WD and MS star, and, in all cases, constraining the detailed physics of these pathways relies on firm knowledge of the frequency and distribution of such systems by component masses, temperatures, separation, eccentricities, and other properties. Because it is now clear that these fundamental statistics of stellar multiplicity are (a) strong functions of stellar properties like mass and chemical composition and (b) not independent of each other (e.g., Badenes et al. 2018; Moe et al. 2019; Mazzola et al. 2020), the *only* way to fully characterize the rich

phenomenology of PCEBs and their associated astrophysical transients is to assemble samples of systems with well-measured parameters that are large enough for robust multivariate statistical analysis. Furthermore, mergers of compact-star binaries are expected to be the most important sources for forthcoming gravitational-wave astronomy.

From an observational perspective, the Sloan Digital Sky Survey (SDSS; York et al. 2000) was efficient at discovering new white-dwarf main-sequence (WDMS) binaries (e.g., Silvestri et al. 2006; Schreiber et al. 2008; Heller et al. 2009; Nebot Gómez-Morán et al. 2009) from optical spectra, but with biases toward systems containing hot WDs and secondaries of late spectral type. Moreover, in Corcoran et al. (2021) we found that some objects classified as WDMS in the SDSS sample are actually young stellar object contaminants. Nevertheless, to date there are more than 3200 WDMS binaries found using SDSS spectra (see Rebassa-Mansergas et al. 2012, for a compilation of these objects). Meanwhile, applying a similar approach to LAMOST (Zhao et al. 2012) optical spectra (e.g., Ren et al. 2018), around new 1000 systems have been reported. However, some of these systems classified as WDMS are actually WD–red giant pairs (Corcoran et al. 2021). Nevertheless, the number of WD binaries with known, *non-MS* secondaries is very small, and this limits the ability to understand the panoply of possible fates of WDMS systems after the secondary star evolves off the MS. Apart from their biases and contamination, another challenge to using the existing databases is that while they provide a large number of candidate WD binary systems, optical spectroscopic surveys typically offer only one radial velocity (RV) epoch, which does not enable characterization of the orbits. Dedicated programs of spectroscopic follow-up have been motivated to address this problem, but the magnitude of the task has limited to a few hundred the number of systems with well-defined orbital parameters (e.g., Schreiber et al. 2008, 2010), and only ∼120 can be considered to be strong PCEB candidates (Lagos et al. 2022).

In the vast majority of known WDMS systems the secondary companion is a low-mass M dwarf, since these are relatively easy to identify from optical colors and spectra. In recent years, there have been efforts to identify WD binaries with more massive FGK-type companions (e.g., Parsons et al. 2016; Hernandez et al. 2021), by combining optical stellar spectroscopic surveys such as RAVE (Steinmetz et al. 2020) and LAMOST with GALEX photometry (Bianchi et al. 2017). Meanwhile, Parsons et al. (2016) obtained Hubble Space Telescope UV spectra for nine systems that confirmed that the photometrically observed UV excess in these systems is indeed caused, in all cases, by a hot compact companion. Clearly broadening wavelength sensitivity to the UV part of the spectral energy distribution (SED) greatly increases leverage in identifying and characterizing a broader variety of WD binary systems.

Here we adopt a similar but even more expansive approach to identifying WD binaries across the H-R diagram, with secondary companions with a broad range of spectral types and in virtually all phases of stellar evolution. Our goal is to perform a new, large, and systematic search for compact binary star systems containing WDs by harnessing information contained in the spectroscopic catalog of the SDSS's (SDSS-IV; Blanton et al. 2017) near-infrared Apache Point Observatory Galactic Evolution Experiment (APOGEE) project (Majewski et al. 2017), cross-matched with data from the optical Gaia (Lindegren et al. 2018) and UV GALEX (Bianchi et al. 2017) space missions. The combination of APOGEE's large *H*-band spectroscopic data set with the UV photometry from GALEX allows us to identify MS F, G, K, and early M stars having significantly bluer GALEX (FUV–NUV) color than can be expected for single MS stars, which is key to our methodology (see Section 2.2). In addition, APOGEE's deliberate focus on sampling evolved stars means that our survey contains WD binary systems with secondary stars amply representing all luminosity classes. Meanwhile, the Gaia database brings not only uniformly measured photometric measurements at optical wavelengths but also critical astrometric measurements helpful for our analysis (e.g., see Section 3.1). We add to the GALEX and Gaia photometry the infrared measurements from the Two Micron All Sky Survey (2MASS) and WISE, which further widens the wavelength range of our SED fitting (see Section 3).

By merging these various surveys, we have created the APOGEE-GALEX-Gaia Catalog (AGGC) of candidate compact binaries containing WD stars. Numbering over 3400 sources, the size of this catalog is comparable to that of previous WDMS catalogs but includes secondary companions in the MS, subgiant branch, RGB, and red clump (RC) phases of evolution, as well as systems that occupy the MS binary and sub-subgiant (SSG) regions of the H-R diagram. Furthermore, it has been shown that WDs in close binaries can acquire nondegenerate envelopes that have radii up to 20 $R_{\oplus}$ (Sokoloski et al. 2006; Lewis et al. 2020; Washington et al. 2021).

The unique properties of the APOGEE catalog confer additional advantages to the AGGC. APOGEE's high-resolution spectroscopy makes possible detailed, multi-element chemical abundance characterization of the binaries, as well as the derivation of precise ($\sim$100 m s^{-1}) RVs. Moreover, APOGEE deliberately visited stars over multiple epochs spanning as long as a decade, which makes it possible to infer orbital information (e.g., derived periods, eccentricities, masses, separations) on the binaries from the time-series RV data. The 252 WD binary systems in the AGGC for which full Keplerian orbits can be derived is already comparable to the previous number so characterized after monitoring campaigns, and the newly characterized systems have been selected in an unbiased way (via standard APOGEE targeting) with secondaries that span almost the full range of stellar evolution. The multi-epoch velocity information for the AGGC makes it a unique tool to explore the evolution of PCEB WD binary properties as the secondary star evolves from the MS all the way to the RC.

The layout of the paper is as follows: Section 2 provides an overview of the creation of the AGGC WD binary candidate catalog, while Section 3 describes the use of the system SEDs to constrain empirically fundamental parameters, such as the effective temperature and the stellar radius of the WD candidates. In Section 4 we explore some of the population distributions for various properties of the WD binary candidates in the AGGC and the creation of the final sample. In Section 5 we demonstrate the usefulness of the newly created catalog of WD binary candidates to address a variety of astrophysical questions related to the evolution of close binaries. In particular, we explore variations in such properties as the WD temperature, the secondary-star metallicity, the

binary period, and the fraction of close binaries as a function of the evolutionary stage of the secondary star. We also discuss the relevance and interpretation of our results. Finally, we draw some general conclusions from a preliminary analysis of the AGGC in Section 6, and we summarize our findings in Section 7.

2. Identification of White Dwarf Stellar Companions with APOGEE, GALEX, and Gaia

The details of the construction of the AGGC and various checks of its veracity are described below.

2.1. Initial Merging of the APOGEE, GALEX, and Gaia Catalogs

The master database from which we will cull our AGGC starts with the APOGEE DR17 catalog (Abdurro'uf et al. 2022). The data were collected using the SDSS telescope located at Apache Point Observatory (Gunn et al. 2006), the du Pont telescope (Bowen & Vaughan 1973) in Las Campanas, and the APOGEE spectrographs (Wilson et al. 2019). The APOGEE selection function for the main survey is simple, with generally only magnitude and color cuts favoring redder stars (Beaton et al. 2021; Santana et al. 2021); as a result, the APOGEE sample is mostly RGB stars (∼70%) and red MS stars (∼30%) (e.g., Zasowski et al. 2017). While these criteria prevent the discovery of individual WDs, the large number of late-type MS stars in APOGEE is a rich parent sample within which to hunt for WD binaries.

The entire APOGEE catalog has already been cross-matched with Gaia eDR3 (Riello et al. 2020) and the 2MASS point-source catalog (Skrutskie et al. 2006) as part of SDSS DR17. From the full APOGEE database (Nidever et al. 2015), we select only stars for which the APOGEE Stellar Parameters and Chemical Abundances Pipeline (ASPCAP) satisfactorily analyzed the combined spectrum of the source to obtain a basic set of stellar atmospheric parameters (e.g., $T_{\rm eff}$, [M/H], $\log g$; García Pérez et al. 2016; Holtzman et al. 2018).[9]

We cross-matched the APOGEE DR17 catalog against the GALEX database (Bianchi et al. 2017). This results in 244,432 stars in common using a separation smaller than 2.″5 on the sky. We then cross-match these stars against the WISE mission catalog (Wright et al. 2010), to procure mid-infrared photometry for our sources. After intersecting all of these catalogs, we create the AGGC as all cross-matched sources that have complete photometric information, defined as having valid entries for the two GALEX bands (FUV–NUV), the three Gaia bands (G, $G_{\rm BP}$, and $G_{\rm RP}$), the three 2MASS bands (J, H, K_s), and all four WISE bands ($W1$, $W2$, $W3$, $W4$). This results in a total of 242,896 objects.

2.2. Identification of White Dwarf Binary Candidates via UV Excess

The comparison of UV photometric data, e.g., as represented by the (FUV–NUV) color from GALEX, to APOGEE-derived temperatures is a sensitive stellar probe for the presence of companions in the form of hot stellar remnants (e.g., Bianchi et al. 2011).

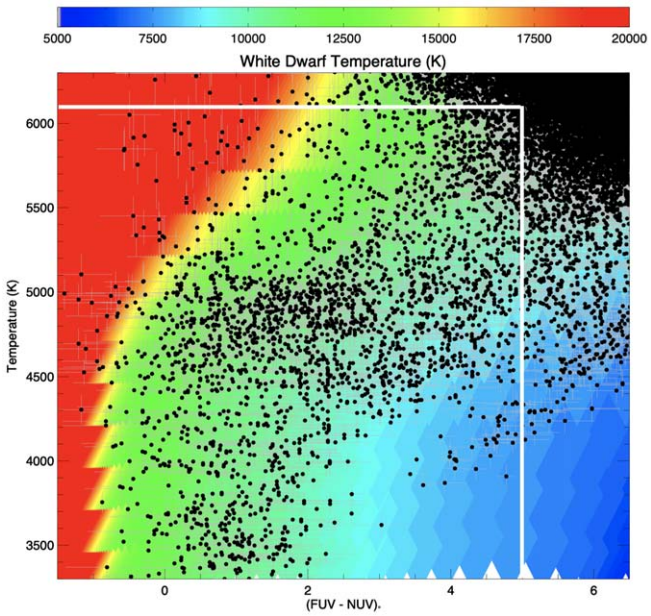

Figure 1. APOGEE-derived effective temperature vs. UV color for the selected stars having GALEX photometry. The figure is color-coded by the nominal WD effective temperatures inferred from ATLAS9 (Castelli et al. 1997) and the WD (Koester 2010) grid of synthetic models for a range of temperatures, assuming MS stars as the red companion. The white line shows the initial, simple selection criterion used for the AGGC, chosen to avoid the single-star locus in the upper right corner of the plot.

Figure 1, which makes such a comparison, clearly shows stellar sources (black points) showing significantly blue UV colors, suggesting the presence of a hot source—a robust filter of candidate binaries with WDs (Maxted et al. 2009; Morgan et al. 2012; Parsons et al. 2016).

To demonstrate how effective is the combination of the GALEX UV color and the spectroscopically derived primary star effective temperature in the elucidation of WD companion properties, the background color scale of Figure 1 shows what might be inferred for the WD effective temperature in the case of a hypothetical binary made from a solar-metallicity, $\log g = 4.5$ MS star modeled with an ATLAS9 (Castelli et al. 1997) atmosphere and a $\log g = 8$ WD modeled with energy distributions from the Koester (2010) grid of synthetic models. To estimate the individual stellar fluxes for the stars, we adopt a solar radius for the non-WD companion and an Earth radius for the WD. This simple exercise immediately elucidates the WD effective temperature distribution we might expect within the AGGC: the largest number of the AGGC sources lie in modeled regions showing an inferred WD effective temperature range of 9000 K $< T_{\rm eff,WD} <$ 15000 K, while a few of the WD binary candidates show potential effective temperatures hotter than 20,000 K.[10]

[9] These are sources for which the APOGEE_ASPCAPFLAG bitmask 23 is not set to "BAD." The latter happens if any of the TEFF, LOGG, CHI2, COLORTE, ROTATION, or SN error parameter bits are set to "BAD," or if any of the above parameters are near a grid edge in the ASPCAP synthetic spectral library used to derive atmospheric parameters (i.e., the flag GRIDEDGE_BAD is set in any PARAMFLAG). See the definitions of APOGEE flags as described at https://www.sdss.org/dr17/algorithms/bitmasks/.

[10] For cooler red star companions, the background color scheme in Figure 1 is not significantly different in the case of red giant companions of $\log g = 1.0$ and radius 10 $R_\odot$, whereas when the red star temperature exceeds about 4500 K, the WD effective temperatures must be correspondingly hotter to result in the same (FUV–NUV) color. Thus, the inferred WD effective temperatures from Figure 1 represent something of a lower limit, for the case of a smaller red star companion.

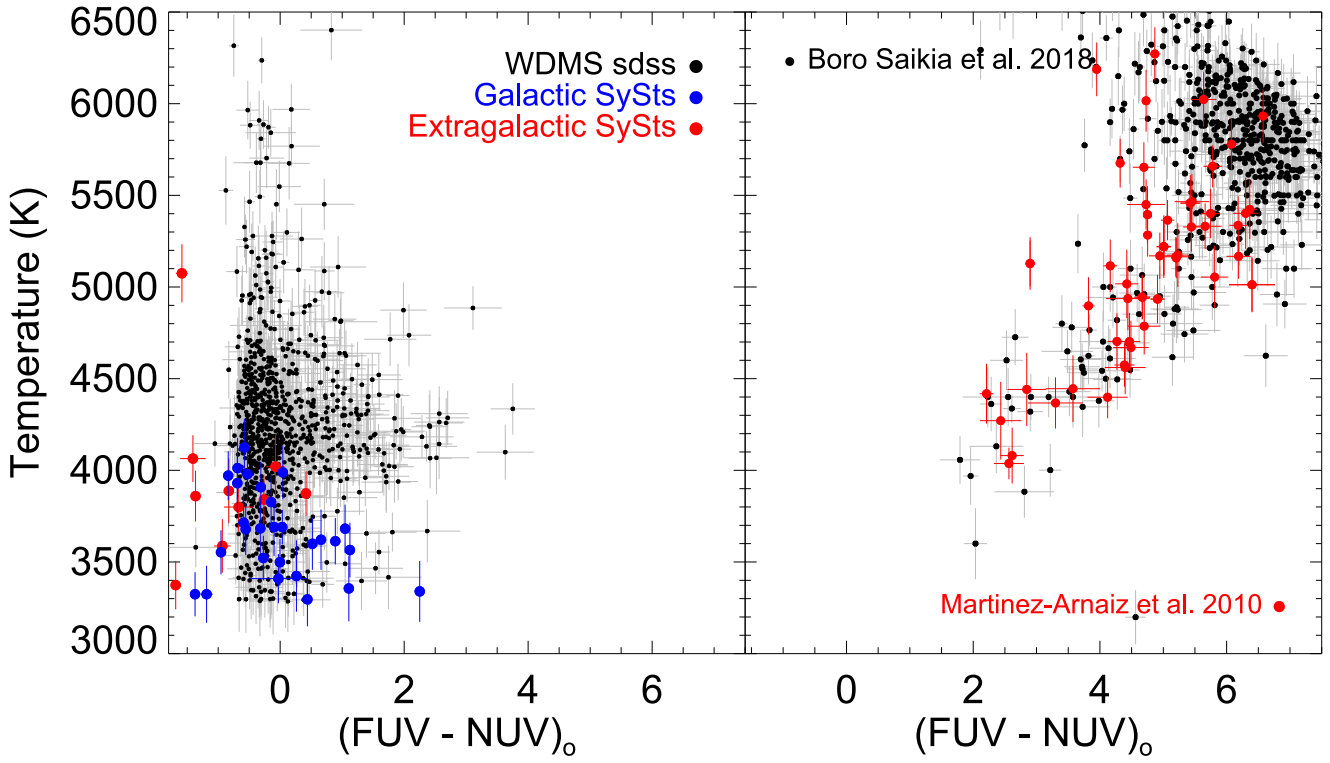

Figure 2. The UV color vs. temperature diagram for WDMS binaries found in the SDSS/SEGUE survey and the galactic and extragalactic symbiotic variables (SySts) reported in Merc et al. (2019; left panel) and chromospherically active stars explored by Boro Saikia et al. (2018) and Martínez-Arnáiz et al. (2010; right panel).

Based on the expected relative locations of single stars and WD binaries in the Figure 1 parameter space (Parsons et al. 2016; Anguiano et al. 2020), systems with $T_{\rm eff} <$ 6000 K and $(\rm FUV–NUV)_o <$ 5 are the most compelling for our purposes. Based on these criteria, we have identified 3414 APOGEE sources that are WD binary candidates with F–M spectral type companions (see also Figure 1 in Anguiano et al. 2020), and that ultimately constitute the final AGGC of WD binary candidates.

The next step is to assess the robustness of this catalog and understand in more detail the types of objects it contains. In the next subsection we describe how we can characterize the WD binary candidates via their SEDs.

2.3. Understanding Subpopulations and Contaminants among the White Dwarf Binary Candidates

There are various types of stellar systems that can populate the Galex-APOGEE diagram. We can use previously characterized systems to understand these subpopulations, as well as to vet the candidates and to identify sources of contamination.

Indeed, one must be cautious that significant GALEX fluxes are not fully reliable indicators of the presence of a WD, as there are other stellar sources that also emit significantly in the GALEX bands (e.g., various types of pulsating stars, chromospherically active stars, young stellar objects, subdwarfs) that could introduce false-positive WD binaries or complicate the interpretation of actual WD binaries. In this subsection, we explore these various issues that play a role in the reliability of the AGGC.

2.3.1. WDMS Binaries in the SDSS

To understand better our methodology and what type of systems populate different parts of the Figure 1 parameter space, we first look at the most up-to-date catalogs of well-established WDMS binaries—the longest-lived, and therefore most common, binaries containing WDs—which are those identified in previous papers using SDSS optical spectra[11] (e.g., Schreiber et al. 2008; Nebot Gómez-Morán et al. 2009; Rebassa-Mansergas et al. 2012). The SDSS catalog contains a net total of 3291 WDMS binaries, which, however, are affected by a mixture of selection effects. Most significantly, because this catalog comprises sources wherein both the WD and MS stars are readily identifiable in the SDSS/SEGUE optical spectra, the SDSS sample is biased toward systems with the greatest temperature separation, namely, systems with relatively hot WDs and cool, M-type dwarf companions.

To demonstrate how the more limited range of SDSS types of WDMS systems contrast with expectations from the AGGC, we cross-matched the SDSS WDMS catalog with GALEX and found 1824 objects having NUV and FUV photometry available. We represent the UV color as a function of the effective temperature of the primary in the left panel of Figure 2 for these objects. Nearly all of the WDMS pairs and the symbiotic binaries (SySts) show a UV color $(\rm FUV–NUV)_o <$ 2.0 and an MS star temperature lower than 4800 K. Contrasting the left panel of Figure 2 with Figure 1 shows the greater sensitivity to a broader range of primary and secondary stars expected in the AGGC.

[11] sdss-wdms.org

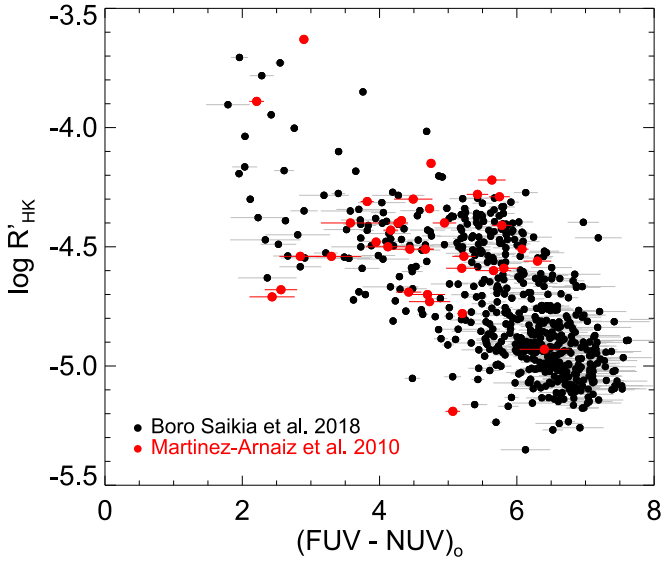

Figure 3. The UV color vs. $\log R'_{\rm HK}$ diagram for the Boro Saikia et al. (2018; black circles) and Martínez-Arnáiz et al. (2010; red circles) catalogs. The most active stars tend to have UV colors $(\rm FUV-NUV)_o < 4.0$.

2.3.2. Stellar Chromospheric Activity

The parent catalog of WD binary candidates from the AGGC sample will contain potential contamination from various sources. For example, Amado & Byrne (1997) reported that single-lined spectroscopic RS Canum Venaticorum (RS CVn) systems, a variable type that consists of close binary stars having active chromospheres, show a UV excess. Hot chromospheres of active stars can result in them possessing quite blue UV colors (e.g., Stelzer et al. 2013; Smith 2018). Furthermore, increased stellar activity in WDMS pairs where the MS is an M dwarf have been reported in optical wavelengths by Morgan et al. (2012), who proposed that such an increase in activity is a result of faster stellar rotation related to possible tidal effects, angular momentum exchange, or disk disruption (see also Jones & West 2016).

To investigate this potential source of contamination, we include two catalogs of stars that, with spectroscopy at blue wavelengths, have detected Ca II H and K line emission but with no obviously detected contribution of flux from a WD at optical wavelengths. Boro Saikia et al. (2018) presented a catalog of chromospheric activity for 4454 cool stars from a combination of archival HARPS spectra and several other surveys, including newly available data from Mount Wilson (Baliunas et al. 1995). In addition, Martínez-Arnáiz et al. (2010) measured chromospheric activity, as given by different indicators throughout their optical spectra, and projected rotational velocities for 371 nearby cool single stars. For the latter study we select only stars classified as "active."

The right panel of Figure 2 shows the effective temperature versus UV color for the two chromospheric activity catalogs mentioned above. We observe a "cool dwarf branch" that shows $(\rm FUV-NUV)_o < 5.0$ and $T_{\rm eff} < 5000$ K. To gain insight into the origin of these stars, in Figure 3 we show the UV color with respect to the ratio of chromospheric Ca II H and K flux to bolometric flux, $\log R'_{\rm HK}$, for the Boro Saikia et al. (2018) and Martínez-Arnáiz et al. (2010) catalogs (black and red circles, respectively, in each of Figures 2 and 3). We observe that nearly all the stars with a color $(\rm FUV-NUV)_o < 5.0$ are cataloged as chrosmopherically active stars. We also observe that activity is the primary driver of the UV color, where MS stars cooler than ∼5000 K have at least some amount of chromospheric activity, while most of the nonactive stars show an $(\rm FUV-NUV)_o > 6.0$. This assessment suggests that the AGGC may have contamination from chromospherically active stars. On the other hand, it may be significant that we do not find active stars in these two independent catalogs with $(\rm FUV-NUV)_o < 2.0$, whereas the bulk of the AGGC catalog has colors bluer than this chromospherically active sequence. Moreover, a star can be chromospherically active *and* have a WD companion. To help further navigate this complicated range of possibilities, we will bring to bear the estimates of stellar radii from the UV GALEX and IR bands together with parallaxes from Gaia eDR3 (Section 3).

2.3.3. Variable Stars

Pulsating stars like Cepheids and RR Lyrae can have blue GALEX (NUV–FUV) colors (e.g., Welsh et al. 2005; Kinman & Brown 2014), and they can be a potential contamination in our candidate WD binary sample. We cross-matched our AGGC sample with a catalog of multiband, time-series photometric characterization of Cepheids and RR Lyrae using Gaia DR2 (Clementini et al. 2019); this catalog contains 150,359 such variables (9575 classified as Cepheids and 140,784 as RR Lyrae stars) distributed across the sky. However, the catalog reaches to the Gaia faint magnitude limit of $G \sim 20.7$, well beyond APOGEE's nominal limits. As a result, we found only five RR Lyrae and four Cepheids in our AGGC sample identified in the Gaia catalog.

We also cross-matched the candidate WD binaries in the AGGC sample against the SIMBAD database (Wenger et al. 2000). The vast majority of our system candidates are classified as "Star" or "High Proper-motion Star," which demonstrates our overall ignorance about these objects (but also that the majority have not been found or studied previously). However, there are six candidate WD binaries classified as "Symbiotic" and four as "Dwarf Nova." Together with the Cepheids and RR Lyrae stars mentioned above, we also find six stars that were previously labeled as "Pulsating Variable Star (PulsV)." In Figure 4 we show the UV color versus $T_{\rm eff}$ diagram with four different panels to explore how specific types of stars currently in the SIMBAD archive occupy this parameter space. The outlined region in the four panels shows the "cool dwarf branch" for chromospherically active stars discussed above (Section 2.3.2). For example, the top left panel illustrates the distributions of Cepheids (black circles), RR Lyrae (black squares), and PulsV stars (triangles) in our candidate WD binary sample. Interestingly, most of the Cepheids and PulsV lie inside the "active branch," whereas the RR Lyrae lie outside this region and are predominantly hotter than 5500 K. We also find seven of our systems to be classified as "T Tau-type star" or "Candidate T Tau-type star." In Figure 4 (top right panel) we show these T Tau (black circles), along with "Young Stellar Objects (YSO)" (triangles) and "Variable Star of Orion Type (Orion-V)" (squares). All of these objects are very young stars in the pre-MS stage (e.g., Mathieu et al. 1991; Kounkel et al. 2018). Despite their UV color (predominantly $\rm FUV-NUV < 1.5$), it is very unlikely that any of these systems have WD companions (Corcoran et al. 2021).

The bottom left panel of Figure 4 shows AGGC objects classified in SIMBAD as "Eclipsing binaries (EB)" (black circles; 77 objects), "Rotationally variable Stars (RotV; 33

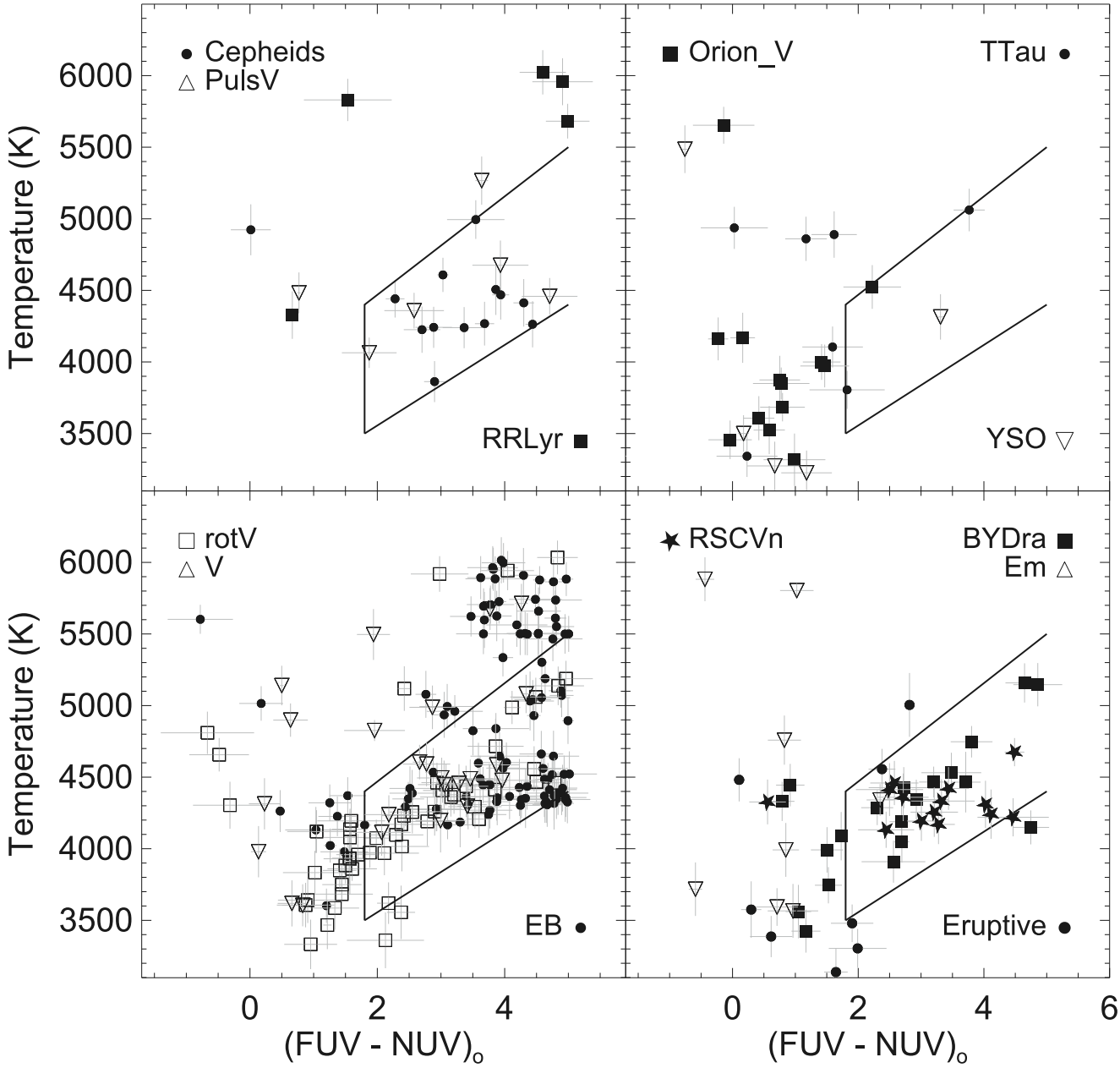

Figure 4. The UV color vs. APOGEE-derived temperature diagram for different types of stars as classified by Clementini et al. (2019) or as listed in the SIMBAD database. The solid lines inside the figures represent the "chromospherically active area." See text for details.

objects)" (squares), and "Variable Stars" (triangles; 22 objects). Most of the stars labeled as EB and RotV are within the "chromospherically active area." Many contact binaries show activity signals, where the binary consists of two low-mass MS stars (mostly F, G, or K spectral type; e.g., Mitnyan et al. 2020, and references therein). Moreover, we observe that some EB and RotV stars could have very blue UV colors, where $(\mathrm{FUV–NUV})_o \sim 1.0$. Furthermore, 14 objects in our sample are listed in SIMBAD as "RS Canum Venaticorum variable (RS CVn)" (star symbols in the bottom right panel of Figure 4). RS CVn are a class of detached binary typically composed of chromospherically active G or K stars (e.g., Biazzo et al. 2006). However, objects classified as RS CVn, with strong Ca II H and K lines in emission, where the hotter component is a WD, are also reported (e.g., Vaccaro et al. 2015). All of the RS CVn but one are inside of the "chromospherically active area" in the color–temperature diagram. We also have 20 objects listed as "Variable of BY Dra type (BY Dra)"; these are a class of object where light variability is caused by axial rotation of a star with a variable degree of nonuniformity of surface brightness due to, e.g., starspots and/or chromospheric activity (e.g., Alekseev 2000). Apparently a close companion is a sufficient, but not a necessary, condition for the occurrence of the BY Dra phenomenon (Bopp & Fekel 1977; Eker et al. 2008). The right panel of Figure 4 also lists objects classified as Emission-line Star (EM; eight objects). These objects are potential novae or CV stars, where we see radiation coming from the accretion disks (e.g., Idan et al. 2010). Finally, we also show objects labeled as Eruptive in SIMBAD as black circles. Some of these variable stars show flares, and the changes in luminosity coincide with shell events or mass outflow in the form of stellar wind (e.g., Tapia et al. 2015).

3. Physical Properties of White Dwarf Companions via Spectral Energy Distributions

Broadband photometric SEDs spanning from the UV to the infrared provide a means both to confirm the presence of a WD in our binary candidates and to constrain empirically the fundamental parameters of the two stars in each system, most importantly the WD effective temperature, and the stellar radius. In this regard, the UV fluxes are critical for constraining the properties of the WD, since it is at these wavelengths that the WD typically dominates the SED.

3.1. Overall Approach

The empirical SED for the AGGC sample is an aid not only in identifying WD binaries but also in deriving system parameters like the WD effective temperature and radius. To create the SEDs, we use the photometric bands from GALEX (Bianchi et al. 2017), Gaia eDR3 (Riello et al. 2020), 2MASS (Skrutskie et al. 2006), and WISE (Wright et al. 2010). Because APOGEE provides reliable information on the red star contributing to the SED, in principle we can use the residual flux to determine the properties (temperature and radius) of the WD. To this end, following the methods laid out by Stassun & Torres (2016), we account for the red portion of the SED (after correcting for extinction by dust) with a Kurucz stellar atmosphere model (e.g., Castelli et al. 1997), where we adopt the stellar atmospheric parameters reported by APOGEE (e.g., Holtzman et al. 2018). If it is assumed that the residual SED flux is attributable to the WD, the properties of that star can be determined by a comparison of that measured residual energy distribution with the hot star spectrum predicted from an appropriately matching model atmosphere. In this case, to interpret the contribution of the WD to the net SED, we use the model WD spectra of Koester (2010).

Once the SED is adequately described, it is possible to ascertain the radii of the constituent stars. For those parts of the SED dominated by one or the other star in the binary, the radius, R, of the corresponding star in units of solar radii is given by conservation of flux, e.g.,

$$R = 4.43 \times 10^7 r (F_\lambda / F_{\lambda,\mathrm{surface}})^{1/2}, \quad (1)$$

where r is the star's distance in parsecs, F_λ is the apparent monochromatic flux, and $F_{\lambda,\mathrm{surface}}$ is the absolute flux at the surface of the dominantly contributing star (see Shipman 1979, for an application of this approach in WDs). In this case, the F_λ are actually obtained using VOSA[12] (Bayo et al. 2008) for the specific photometric bands mentioned above, while to compute the absolute flux at the surface of the star, $F_{\lambda,\mathrm{surf}}$, we use (as mentioned above) either the model WD atmosphere spectra of Koester (2010) or the Kurucz stellar atmosphere model (e.g., Castelli et al. 1997), as appropriate. In practice, to measure the WD radii, we use the fluxes from the two GALEX bands, while to measure the radius of the secondary we use the fluxes from the 2MASS bands along with the W1 and W2 bands from WISE.

Note that the SED-fitting procedure implicitly assumes that both the cool component and the hot component are single objects. This assumption naturally breaks down for some types of systems, such as triple systems where the cool component is in fact itself an unresolved binary. The most extreme case is that for which the cool component is an equal-mass binary, such that the observed flux is a full factor of 2 larger than for a single star. In that case, the cool component will appear to have an inferred radius that is overestimated by a factor of $\sqrt{2}$. As we discuss in Section 4, only 192 systems are affected. Most importantly, this does not impact the derived parameters for the WD component, unless the system is a triple with two WDs, which is extremely unlikely.

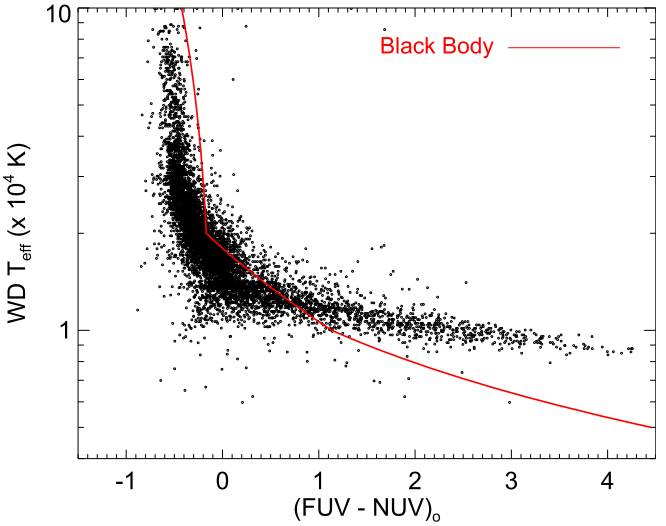

Figure 5. The dereddened UV color vs. temperature distribution for confirmed WDs in the SDSS. The red line shows expectations for a blackbody. The blackbody was generated by the synthetic models in the Virtual Observatory facility (VOSA), and the steps in temperature jump from 50 to 1000 K for temperature hotter than 20,000 K; the log scale amplifies this effect.

The effective temperature of the possible hot companion in our system candidates is another parameter we can extract from the SED analysis. This temperature is the primary driver of the GALEX UV color. To understand the relation between the (NUV–FUV) color and the temperature of the WD, we use the SDSS DR12 WD catalog with spectroscopic temperatures used in Anguiano et al. (2017) to create the distribution in Figure 5. In this case, the WD effective temperatures were derived (Kepler et al. 2016) by fitting the Balmer lines sampled by the SDSS spectra with the one-dimensional model atmosphere spectra of Koester (2010). However, we note a discrepancy between the Kepler et al.–derived color–temperature relation for the SDSS WDs and expectations from a blackbody (red line in Figure 5), with those differences increasing in the cool regime. We use the synthetic photometry and temperature listed in VOSA (Bayo et al. 2008) for the blackbody in the UV bands. This discrepancy could be related to the effect on temperature of convective atmospheres, which is important for cool WDs (e.g., Tremblay et al. 2013) and demonstrates that invoking a blackbody to represent the WD contribution to the SED may lead to systemic offsets in derived temperatures. As may also be seen in Figure 5, the UV GALEX color saturates to a nearly constant value for WDs with $T_{\mathrm{eff}} > 30{,}000$ K. While this may caution one from trusting SED fitting at such hot temperatures, our procedure here, which makes use of actual WD models rather than simple blackbodies, does at least produce results for the hottest WDs (see Figure 9 below) that are more in line with the Kepler et al. (2016) methodology shown in Figure 5.

In the end, we derived the WD radii and effective temperatures for each candidate WD binary by simultaneously

[12] http://svo2.cab.inta-csic.es/theory/vosa/

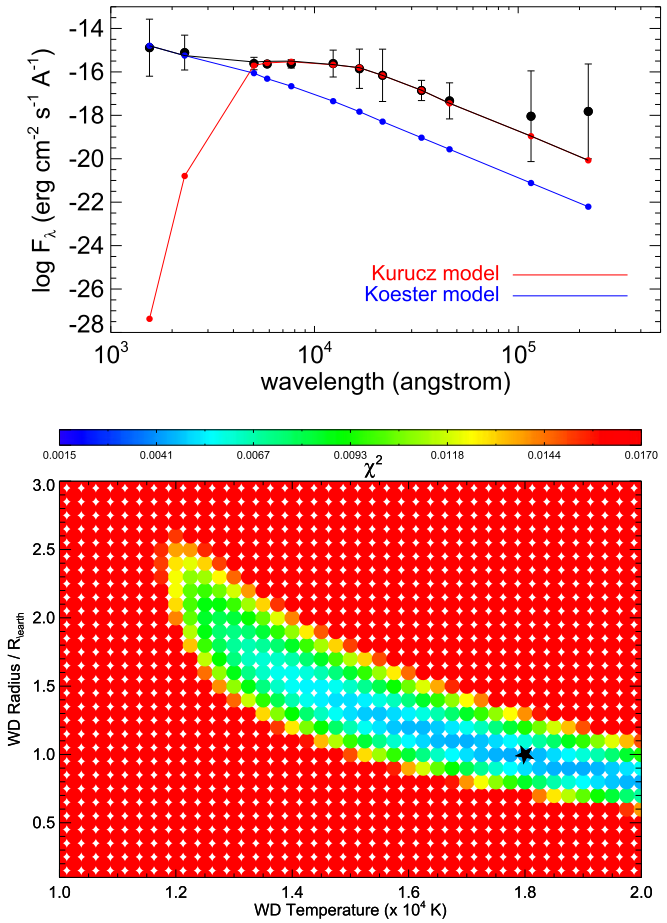

Figure 6. Top panel: the best-fitting SED (black line) for a WDMS binary using GALEX, Gaia, 2MASS, and WISE broadband photometry (black circles). The red line is the best Kurucz model (Castelli et al. 1997) fit for the secondary, while the blue circles/line represent the best-fitting Koester (2010) model for the WD. Bottom panel: WD temperature–radius plane color-coded by the χ^2 value. The blue color indicates the lowest χ^2 value.

fitting to the observed SED the combination of a single, APOGEE-motivated red star model and a variety of blue star model contributions, where temperature and radius are the free parameters. The best fit is found through χ^2 minimization, where the latter is given by

$$\chi^2 = \sum_{i=1}^{n} \frac{(O_i - E_i)^2}{E_i}, \quad (2)$$

where E_i is the sum of flux from the models for the two stars, O_i is the SED, and we estimate the agreement between the observed and the expected distributions for all 10 of the individual photometric bins, i, utilized (see below).

While for the secondary star we adopt the stellar parameters ($T_{\rm eff}$, [M/H], $\log g$) given by APOGEE DR17, in practice the SEDs are primarily sensitive to $T_{\rm eff}$, with little or no influence by (i.e., and therefore little sensitivity to) the overall stellar metallicity or surface gravity. In the fitting of the secondary-star SED we use all the photometric bands except the WISE W3 and W4 bands, which often show a clear deviation from the models for the nominal secondary-star temperature (see the top panel of Figure 6 for a typical example). IR excesses observed in these bands may suggest the presence of warm dust around the star (e.g., Da Costa et al. 2017, and references therein). For the SED extinction correction, we deredden the observed flux using the reddening curve from Fitzpatrick (1999) parameterization, which is valid from the IR to the FUV. The $E(B-V)$ value is given for each source in the GALEX catalog (Bianchi et al. 2017), based on the extinction maps of Schlegel et al. (1998). A typical "average" extinction law for the diffuse interstellar medium, where $R(V) = 3.1$, is assumed.

Practically, for the blue side of the SED, the constraints for our χ^2 approach are the effective temperature and the radius of the WD. We use only the models with $\log g = 8.5$ from the Koester WD models (Koester 2010) because the WD surface gravity information encoded in the two GALEX bands is negligible. The effective temperature coverage in the Koester models goes from 5000 to 80,000 K, but the grids do not always have a uniform coverage of all of parameter space. In this case, the temperature steps are only 250 K from 5000 to 20,000 K, then 1000 K steps are used from 20,000 to 40,000 K, and then, finally, 10,000 K steps are implemented from 40,000 to 80,000 K. However, as pointed out earlier, because of the saturation of the (FUV–NUV) color (Figure 2), for WDs hotter than 30,000 K we cannot retrieve reliable temperatures from the UV GALEX bands anyway; fortunately, however, the vast majority of WDs have temperatures cooler than 30,000 K (see Figure 5).

Just as for the secondary star where the radius is given primarily by 2MASS and WISE bands, we use only the FUV and NUV GALEX bands to estimate the WD radius because the contribution in the UV flux from the secondary's photosphere is negligible. For each given temperature in the WD model grid, we test different radii from 0.1 to 500 $R_\oplus$ in steps of 0.1 $R_\oplus$, following Equation (1). Estimated stellar distances, r, came from Gaia eDR3 parallaxes and the Bayesian isochrone-fitting code StarHorse (Santiago et al. 2016; Queiroz et al. 2020).

Figure 6 shows a representative final SED fitting, together with the χ^2 surface in the two-dimensional parameter space of WD temperature and radius, for a confirmed WDMS binary.[13] The SED in the top panel shows the best combined total fit (black line) to the observed fluxes (black circles) using the Kurucz model for the secondary (red line) and the Koester model for the WD (blue line).[14] The bottom panel shows the χ^2 distribution as a function of WD temperature and radius. The ridge of blue color in this plot represents the valley of low χ^2 values and hence the WD model that results in the best fits between the model and the data. To avoid potential outliers and/or upper limits, the χ^2 is calculated using all data points except W3 and W4 from WISE. The lowest χ^2 value for this SED fitting is represented as the black star symbol, and for this particular system it indicates that this occurs for $T_{\rm eff} \sim 18{,}000$ K and $R \sim 1.0\,R_\oplus$.

The radius uncertainties for a given band, ϵR_λ, are determined by error propagation of Equation (1), that is,

$$\epsilon R_\lambda / R = [(\epsilon F_\lambda / 2F_\lambda)^2 + (\epsilon r / r)^2]^{1/2}, \quad (3)$$

where we have assumed that the uncertainties associated with the models are negligible and so set $\epsilon F_{\lambda,\rm surf} = 0$. Thus, the radius uncertainties depend on the uncertainties in the observed fluxes, ϵF_λ, and the uncertainties in the stellar distances, ϵr. Like we did for the stellar radius, we use 2MASS and WISE

[13] SDSS J232217.42−005725.5 (Eisenstein et al. 2006).

[14] The original models have been rescaled to $4\pi \times$ Eddington flux in units of erg cm^{-2} s^{-1} Å^{-1}.

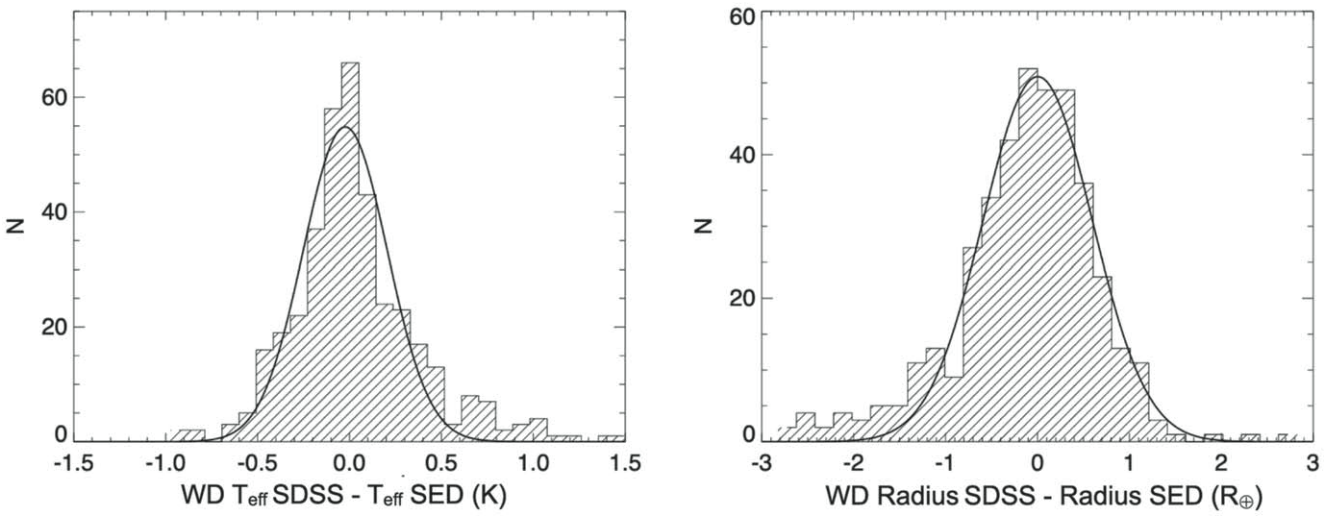

Figure 7. Histogram of the discrepancies between the temperature and the radius derived in the SDSS spectra and those derived in this work using an SED-fitting procedure. A fit with a simple Gaussian (black line) reveals small offsets in the results coming from the two methods and a dispersion of ∼2200 K for the temperature and ∼0.6 $R_\oplus$ for the WD radius.

bands for the secondary and FUV and NUV GALEX bands to estimate the uncertainties for the WD. We estimate ϵR using the average ϵR_λ for the bands used in each stellar component. To obtain the temperature uncertainties, we first considered using the radius uncertainties and the χ^2 value: from the $R \pm \Delta R$ values in the temperature–radius plane (see bottom panel in Figure 6) we select the lowest χ^2 values for the corresponding radii as the lower and upper temperature values. However, the resulting uncertainties were in our assessment overly optimistic; hence, we instead adopt the comparison between our SED estimates and the SDSS spectroscopic values, for which we find $\sigma_T \sim 2200$ K.

3.2. Validation against SDSS WDMS Binaries

We tested the WD effective temperatures and radii derived using this SED-fitting procedure against these same parameters as derived independently for the SDSS WDMS pairs discussed in Section 2.3.1. To do so, for the SDSS WDMS systems we use the stellar distances derived from Gaia eDR3 parallaxes with the probabilistic approach that uses a prior constructed from a three-dimensional model of our Galaxy developed by Bailer-Jones et al. (2021). In the SDSS catalog, WD parameters like $T_{\rm eff}$ and $\log g$ are estimated using the best-fitting template and the Balmer lines in the SDSS optical spectra (Schreiber et al. 2008; Nebot Gómez-Morán et al. 2009; Rebassa-Mansergas et al. 2012). They also estimated the mass and the radius of the WD by using theoretical cooling models (e.g., Bergeron et al. 1995), together with the stellar parameters determined from the best line profile fit ($T_{\rm eff}$, $\log g$). Because, obviously, $\log g$ depends both on mass and on stellar radius, the SDSS WD masses and radii must rely on a theoretical mass–radius relation (e.g., Provencal et al. 1998). For the comparison exercise, we need to bear in mind that while our radius estimation for the confirmed SDSS WDMS relies mainly on distances and on the ratio between the apparent and absolute flux, the listed radius in the literature relies on the estimation of $\log g$ from the Balmer lines in the SDSS spectra and the theoretical mass–radius relation for WDs. Hence, with this validation exercise we also compared two different approaches to estimate the WD radius in these binary systems.

With the temperatures and radii for the SDSS WDs in hand, we can compare them to the same values derived from the SED analysis. The left panel of Figure 7 shows the histogram of discrepancies between the WD temperatures derived using the SED analysis and the WD temperature estimated from the SDSS WDMS spectra (e.g., Schreiber et al. 2008; Nebot Gómez-Morán et al. 2009; Rebassa-Mansergas et al. 2012). Fitting a simple Gaussian to the histogram of discrepancies, we find a small offset of about $\mu_{T_{\rm eff}} \sim -200$ K and a spread of $\sigma_{T_{\rm eff}} \sim 2200$ K (see Figure 7). Similarly, in the right panel of Figure 7, we fit the distribution of discrepancies between the WD radii (in Earth radii) calculated for the SDSS optical spectra as described above and those found from the SED analysis. Here we find no significant offset and a spread of $\sigma_R \sim 0.6\ R_\oplus$ from the Gaussian fitting. Thus, we see from these overall good agreements of our calculated WD $T_{\rm eff}$ and radius values with those previously found by other surveys that our SED-fitting procedure is reliable, at least for the WDs in WDMS binaries of the type found in the SDSS catalog.

4. Results: A Comprehensive Catalog of Compact Binaries with White Dwarfs

In this section we present the AGGC to study WDs in close binaries. Table 1 represents the first four lines of our WD binary sample. Together with the APOGEE and Gaia EDR3 IDs and the $T_{\rm eff}$, $\log g$, and radius for the secondary, the table shows the estimated WD $T_{\rm eff}$ and radii in $R_\oplus$. In the next section, we discuss some physical features of the sample like the WD $T_{\rm eff}$ and radii.

4.1. Radius and Temperature Distributions

Figure 8 shows the derived stellar radius distributions for the MS (black line) and RG (red dashed line) secondary stars (left panel, for which the units shown are solar radii) and those for the WD candidate primaries (right panel, for which the units shown are in Earth radii). We broke the distribution between MS and RG using the APOGEE surface gravity, where we use $\log g > 4$ to select MS and $\log g < 4$ for the subgiants and RG.

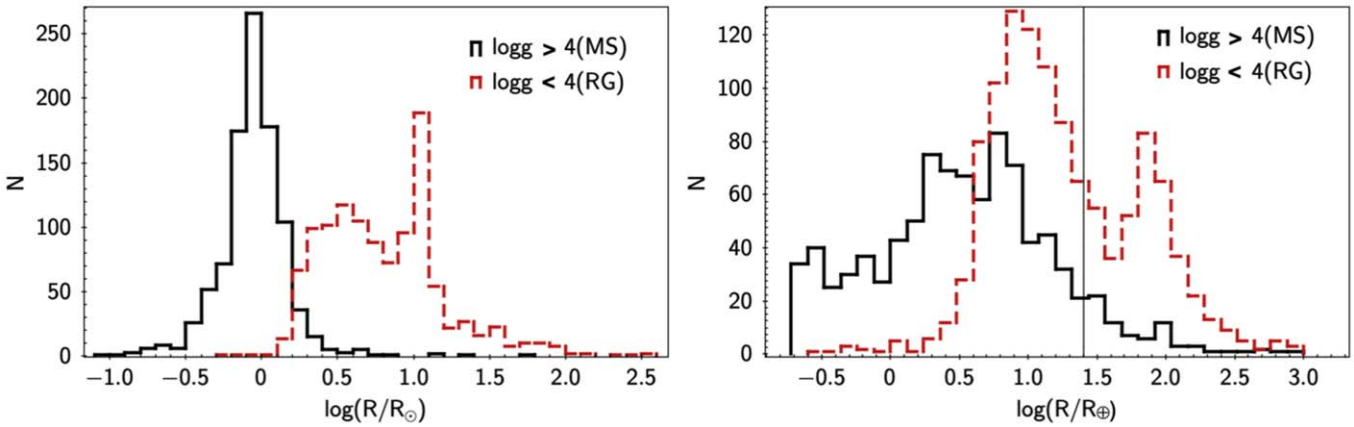

Figure 8. Left panel: stellar radius logarithmic distribution for the MS and RG star secondaries in solar radii. Most of the MS stars have radius close to 1 $R_{\odot}$ (black line). We also have subgiants and giant star secondaries with a large range in radius (red dashed line). We use the APOGEE surface gravity to select MS and RG objects, as indicated in the legend. The distribution shows a group of giants with $R \sim 10\ R_{\odot}$, associated with the RC. Right panel: stellar radius distribution for the WD candidates, where the units are in Earth radii for MS (black line) and RG (red dashed line). The vertical black line represents the value $R = 25\ R_{\oplus}$. The number of WDs with $R < 3\ R_{\oplus}$ is much larger for MS than for RG. In the RG distribution most of the WDs have $R \sim 9\ R_{\oplus}$.

Table 1
WD Binary APOGEE DR17 Catalog

APOGEE ID	Gaia EDR3 ID	R.A. (J2000) (deg)	Decl. (J2000) (deg)	WD $T_{\rm eff}$ (K)	Sec $T_{\rm eff}$ (K)	Sec log g (cgs)	$R_{\rm WD}$ ($R_{\oplus}$)	$R_{\rm sec}$ ($R_{\odot}$)
2M00001362−1913042	2413936998069050496	0.0568	−19.2178	10683	5555	4.3	5.2	1.1
2M00031637+0203553	2739046437325768704	0.8182	2.0653	10656	4747	2.9	9.7	6.7
2M00042113+0109145	2738372917734134144	1.0881	1.1540	11810	4838	3.4	2.9	3.1
2M00081185−5220420	4972421528506663552	2.0494	−52.3450	9796	3632	4.7	0.3	0.4

The distribution of MS secondary stars shows a clear peak near about one solar radius and ranges from 0.1 to 3.5 $R_{\odot}$. While in the RG we have a very clear peak around $R \sim 10\ R_{\odot}$, which is dominated by RC giants, the radii for the subgiants and RG show a range from 1.5 to ∼300 $R_{\odot}$ (see also Figures 10 and 11). In the right panel of Figure 8 we also have the derived stellar radius distributions for the WDs. The two histograms represent the MS (black line) and RG (red dashed line) secondaries, respectively. Interestingly, the number of WDs with $R < 3.5\ R_{\oplus}$ is much larger for the MS objects than for the RG. The WD stellar radius distribution for the RG shows also another peak where the radius of the WD candidate is 100 $R_{\oplus}$. These objects will be removed from our final WD binary sample (see also Figure 10). The vertical line in the right panel of Figure 8 represents $R = 25\ R_{\oplus}$, an upper limit for our WD binary sample.

Figure 9 shows the WD temperatures and radii against the GALEX UV colors, for WD radii up to $20\,R_{\oplus}$. The WD temperature derived using the individual SEDs agrees with the expected UV color for the individual WDs, as we discussed for SDSS WDs in Figure 5. Moreover, as shown by the color-coding for calculated radius of the candidate WD in the system, the systems with WDs hotter than 10^4 K are dominated by those with radius smaller than 5 $R_{\oplus}$, whereas the systems with temperatures cooler than 10^4 K are dominated by objects with a larger stellar radius than the expected radius range for a WD. However, WDs with radius around 20 $R_{\oplus}$ have been reported for WD binary systems (e.g., Sokoloski et al. 2006; Lewis et al. 2020); such an inflated radius for a WD can indicate the presence of a disk around the star.

We use the derived photometric stellar radii to build the MS/RG radii versus WD radii diagram shown in Figure 10. This diagram can be used to refine our selection of WD binary candidates. The radii derived using GALEX bands appear in Earth radius units, while the radii using IR bands are in solar units. The top panel of Figure 10 shows the sample of bona fide WDMS binaries found in the SDSS (Section 2.3.1, Figure 2). The number of SDSS WDMS pairs with $T_{\rm eff} > 4500$ K drops suddenly because the flux from the secondary can dominate the optical spectrum, obscuring the flux from the WD. This bias should be less severe in the present exercise, where we use the GALEX UV bands to identify the WD. For instance, we find WD binaries where the primary can be hotter than ∼4500 K (see black points in Figure 1). The SDSS WDMS sample is a useful guide to where some confirmed WD binaries should appear in the radius–radius diagram. We highlight the limit to where these objects live using a red line in the figure. This population is dominated by stars with $R < 0.8\ R_{\odot}$.

In the middle panel of Figure 10 we show the AGGC sample for those objects for which we have calculated the radii using SEDs and APOGEE DR17 StarHorse distances along with Gaia eDR3 parallaxes. The AGGC sample clearly consists of systems with MS secondaries with $R < 2\ R_{\odot}$, as well as with subgiants and giant star secondaries with $R > 2\ R_{\odot}$. We also see a clear signature of an RC population, as the spike of systems visible at $R \sim 10\ R_{\odot}$.

Finally, we also show in Figure 10 (bottom panel) the locus of *chromospherically active stars* from the Boro Saikia et al. (2018) catalog discussed in Section 2.3.2. We found that stars in the "cool dwarf branch" going from ∼5000 to ∼3900 K discussed in Figure 2 show a radius derived from the UV bands with $R < 10\ R_{\oplus}$. Thus, while the chromospherically active sources primarily mimic single stars in Figure 10, some also resemble WD binaries. However, such stars may not be "contaminants" but systems for which chromospheric activity

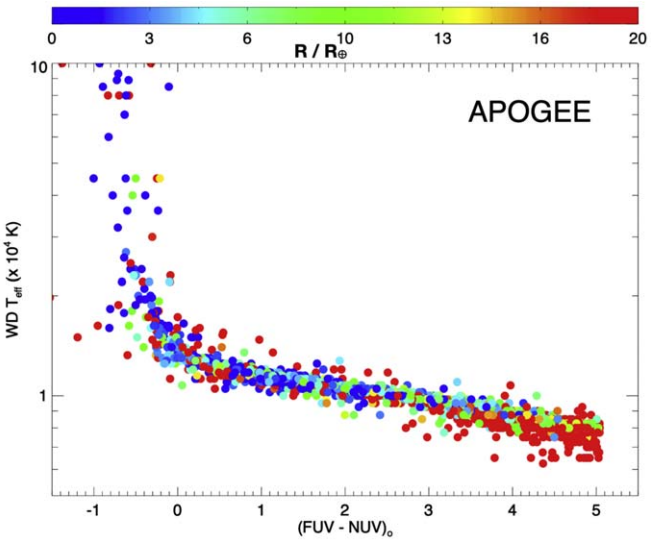

Figure 9. Comparison between the WD temperature derived using SED fitting and the (FUV–NUV) GALEX color. The figure is also color-coded with the WD radii. Stars with $R_{\rm WD} > 20\ R_{\oplus}$ tend to have $T_{\rm eff} < 10^4$ K.

itself has been incited by interaction with a close WD companion (e.g., Bleach et al. 2002).

4.2. Temperature–Radius Diagram

We investigate the APOGEE-derived effective temperature of the secondary star as a function of UV color in the left panel of Figure 11; the systems represented in this figure are color-coded by the derived stellar radius for the WD candidate. Meanwhile, the right panel of Figure 11 shows a *temperature–radius diagram*, given by the derived radius of the secondary as a function of the difference between the WD temperature and the secondary. The points in this figure are also color-coded by the derived WD radius.

Together, the two panels of Figure 11 reveal that the majority of systems with $R > 25\ R_{\oplus}$ for the potential WD have $(\mathrm{FUV-NUV})_{\circ} > 3.5$, a color value that corresponds to a WD $T_{\rm eff} \leqslant 9000$ K (see also Figure 5). This suggests that WD binary candidates with the WD $T_{\rm eff} \leqslant 9000$ K are very likely dominated by a non-WD companion. By contrast, the number of WDs detected in SDSS with $T_{\rm eff} < 10^4$ quickly drops (e.g., Kepler et al. 2016, and also Figure 5 in this work), suggesting that for $(\mathrm{FUV-NUV})_{\circ} > 3.5$ the number of non-WD binaries should be significant, as is suggested, in any case, by the large radii found in this exercise. As may be seen in the right panel of Figure 11, nearly all the stars with $R < 1\ R_{\odot}$ present an $R < 10\ R_{\oplus}$ for the WD candidate. In addition, objects where the temperature discrepancies are smaller than 3500 K are dominated for objects with radii larger than $25\ R_{\oplus}$.

4.3. Final Sample

These radius–radius and radius–temperature diagrams discussed above provide a useful guide for creating a relatively clean sample of WD binary candidates within the AGGC sample. The red line shown in several panels of Figure 10 represents our chosen criterion to select the highest-probability WD binaries in the AGGC sample, mindful of the loci traced by the SDSS WDMS binaries and those traced by the presumed single stars. A total of 1806 AGGC stars fall below the red line

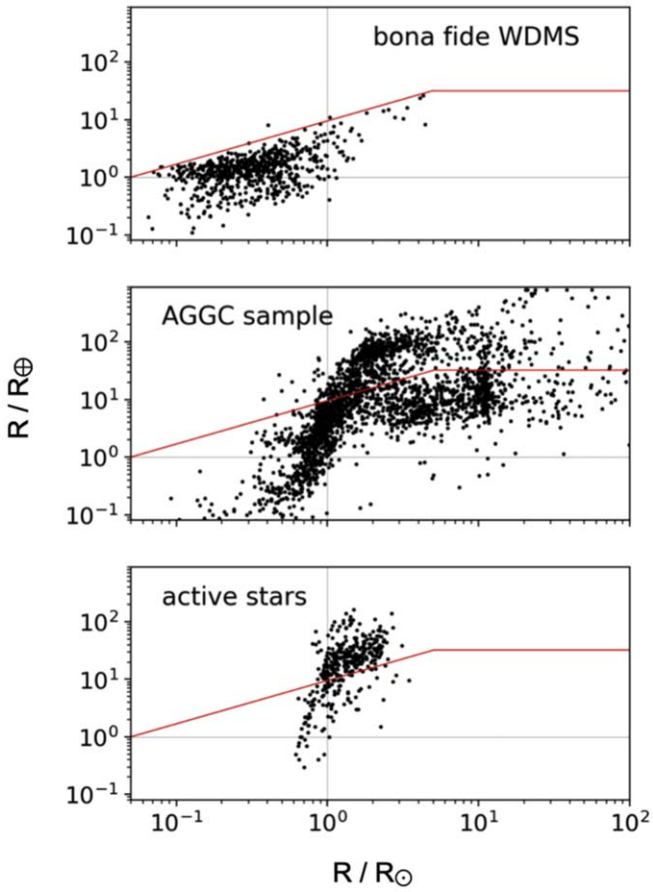

Figure 10. APOGEE-derived radii for the non-WD stars vs. the nominal WD radii inferred from SED fitting (Section 2.4) for SDSS optical WDMS candidates (sdss-wdms.org; top panel), our parent sample of WD binary candidates based on Figure 1 (middle panel), and chromospherically active stars from Boro Saikia et al. (2018; bottom panel). In each panel, the red line represents a criterion, guided by and separating the loci of most single stars, most chromospherically active stars, and almost all bona fide WD stars from SDSS; the best AGGC stars will lie below this line.

and constitute this more reliable sample of WD binary candidates.

5. Discussion: Color–Magnitude Diagram and Compact Binary Evolution

As a demonstration of the potential for the AGGC to address numerous scientific questions, in this section we do a pilot exploration of the color–magnitude diagram (CMD) for the selected WD binary candidates described above and investigate how various properties of WD binaries vary as a function of the evolutionary state of the secondary star in the system. To build the CMD, we use (a) the effective temperatures from APOGEE DR17 (Abdurro'uf et al. 2022), (b) the StarHorse distances (Queiroz et al. 2020) including Gaia eDR3 parallaxes (Lindegren et al. 2020), and (c) the near-infrared H (1.25 μm) bandpass apparent magnitudes from 2MASS (Skrutskie et al. 2006) to compute the absolute magnitude M_H corrected from (d) reddening using the extinction values provided in the StarHorse catalog. When distances from the StarHorse catalog are not available for our objects, we use the photogeometric distances listed in Bailer-Jones et al. (2021).

The resulting CMD of the WD binary candidates is shown in Figure 12, which is color-coded by the inferred effective

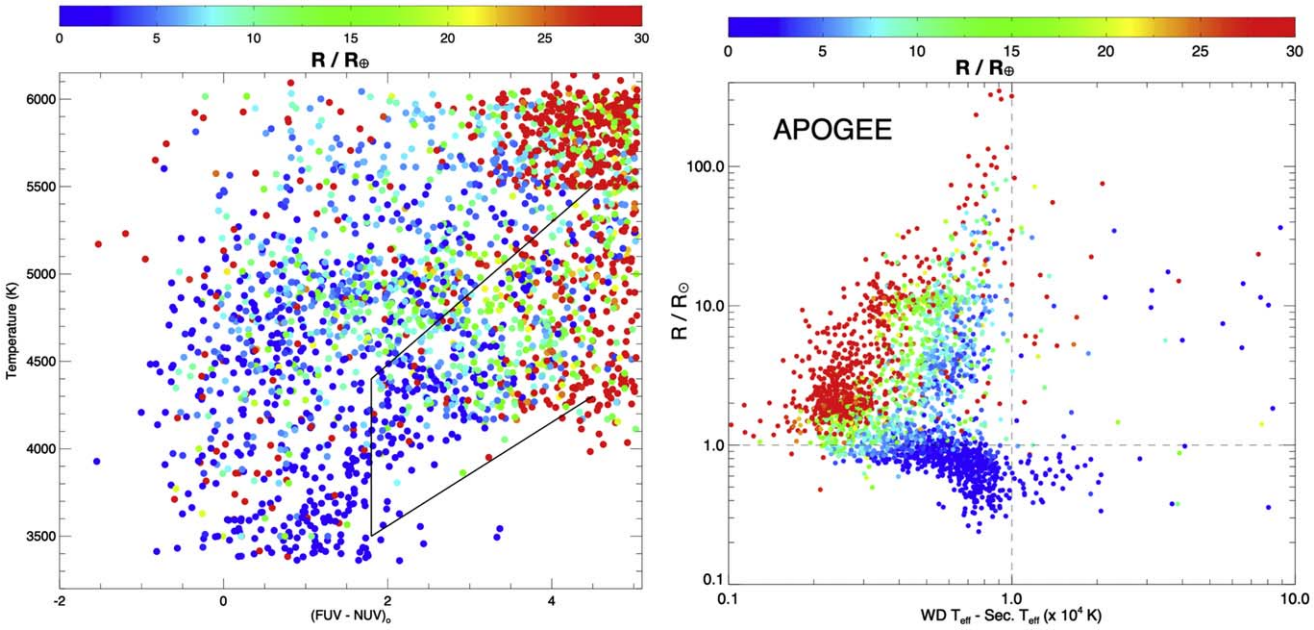

Figure 11. Left panel: APOGEE-derived effective temperature vs. UV color for the AGGC sample. The figure is color-coded by the estimated WD radii. The vast majority of objects with $(\mathrm{FUV}-\mathrm{NUV})_o < 3.5$ in the AGGC show a potential WD where the radii are $R < 10\ R_\oplus$. Right panel: the temperature–radius diagram, given by the derived radius of the secondary as a function of the difference between the WD effective temperature and the secondary. The figure is color-coded by the derived WD candidate radius.

temperature of the potential WD in these pairs (see Section 3). The figure shows a well-defined MS, a good number of subgiants, and also a well-defined RGB, together with a prominent RC. Some WD binary candidates appear in the binary sequence above the MS; in the case of our WD companion population, these would likely be triple-star systems comprising the visible APOGEE MS star, the WD companion, and another luminous companion comparable in brightness to the APOGEE MS star. Finally, we note a number of systems populating the space between the MS and the subgiant branch, with $T_{\rm eff} \sim 4500$ K and $M_H \sim 1$. These would appear to be so-called SSGs; we return to discuss this interesting population in Section 5.1.

A sample of highly likely WD binaries identified across the CMD is an important step toward furthering our understanding of compact binary evolution. One example where improvement is possible (already discussed in Section 3) is that SDSS WDMS identified using optical spectra alone are less able to discern bimodal SEDs when the MS star is hot, and thus such a resulting WD binary survey is strongly biased to those with very late type companions. Furthermore, our knowledge of the fundamental statistics of stellar multiplicity, e.g., multiplicity fraction and period distribution, is still poorly understood, especially for evolutionary stages after the MS and for a volume of study larger than the solar neighborhood (e.g., Badenes et al. 2018, and references therein). In the following section we analyze some properties of our binary sample across the H-R diagram in an initial, pilot assessment of this very rich database.

5.1. Properties of White Dwarf Compact Binaries across the H-R Diagram

We first examine and compare properties like the WD temperature and the overall metallicity of the secondary in different regions of the CMD. Figure 13 shows the WD binary CMD presented in Figure 12 but now broken up into areas corresponding to WB binary systems containing secondaries on the upper RGB, the RC, the lower RGB and subgiants, the MS, the MS binary sequence, and the SSGs. On the right of Figure 13 we have two panels. The top panel shows the cumulative distribution function (CDF) for the WD temperature, while the lower one shows the CDF for the APOGEE overall metallicity. We find that the upper RGB shows the largest number of hottest WDs, followed by the MS population, compared to the other regions of the CMD. Interestingly, the RC temperature distribution shows a WD temperature distribution closer to the lower RGB region. The MS binary sequence suggests that these systems are triplets where one component is a WD; its WD temperature distribution is similar to the MS sample. The SSG CDF also shows a different distribution with respect to the other populations. In the bottom panel we have the CDF for the metallicity. We find that the metallicity distribution function for the upper RGB (black solid line) differs from the rest of metallicity distributions from different populations in the CMD.

The number of metal-poor systems ($[\mathrm{Fe/H}] < -0.7$) on the upper RGB is much larger than for the RC and the lower RGB. Such a metal-poor tail for the upper RGB compared to other regions in the CMD cannot just simply be explained because the volume of study is larger and there are a larger number of halo objects. To understand better the discrepancies we find for the overall metallicity of the WD binaries on the upper RGB and to gain insights into the potential abundance variations induced in the secondary star during the CE phase, it is worthwhile to investigate the differences across the CMD in the metallicity distribution function between systems dominated by WD binaries and a control sample dominated by single stars.

To build a closely matching, single-star control sample, we subsampled the APOGEE database using the following flags

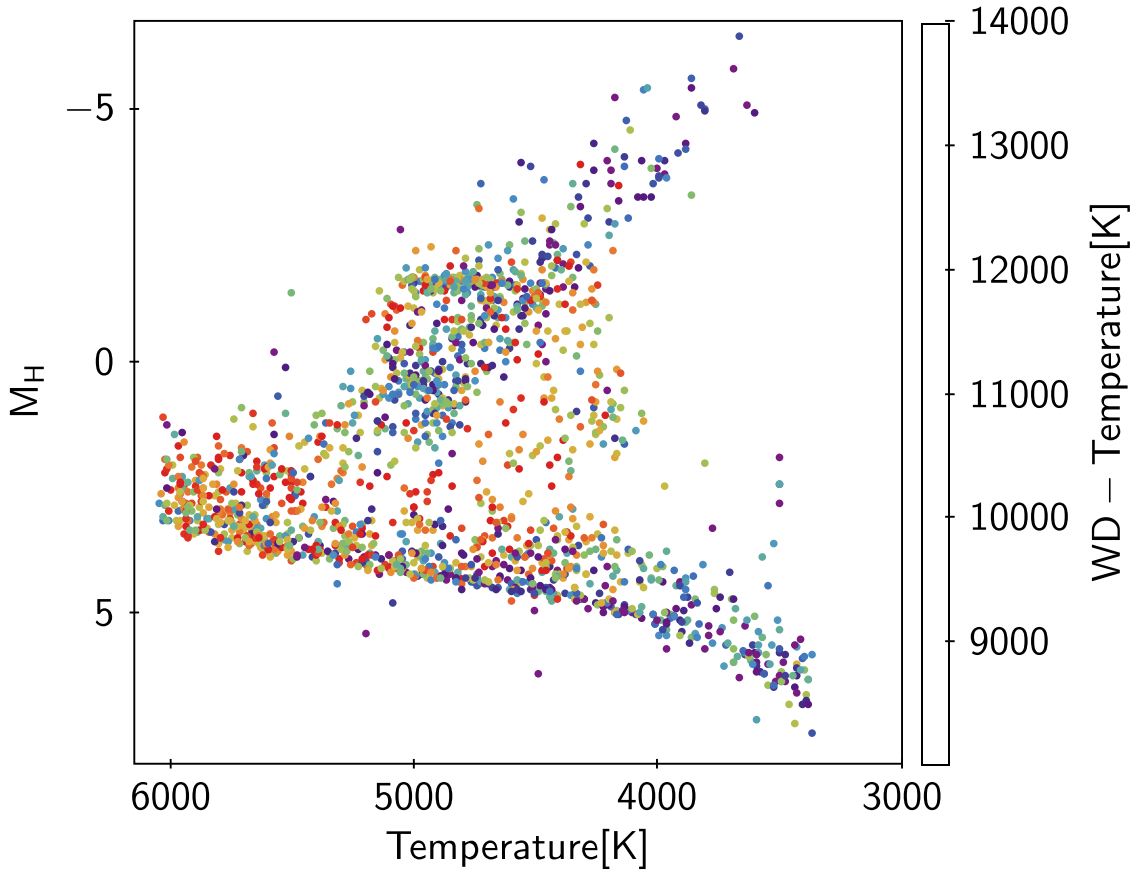

Figure 12. H-R diagram for the AGGC, with APOGEE-derived temperatures and *H*-band luminosities from 2MASS photometry+Gaia parallaxes. Sources are color-coded by the inferred WD temperature from the SED fitting (Section 3).

and selection criteria:

```
NVISIT > 5
VSCATTER < 300 m s^-1
BAD_PIXELS
VERY_BRIGHT_NEIGHBOR
LOW_SNR
STAR_BAD
```

This gives a total of 12,443 APOGEE targets that should be dominated by single stars. A cross-match of this "single-star" catalog with the double-lined spectroscopic binary sample identified by Kounkel et al. (2021) yields only 26 stars in common, which we remove. In addition, because we want to build a sample of stars that is as random and unbiased as possible, whereas the APOGEE survey has a number of focused science programs that target specific classes of objects (Beaton et al. 2021; Santana et al. 2021), we remove targets in fields associated with these special programs. This, for example, removed from consideration the stars from a number of Milky Way satellite galaxies targeted by APOGEE, which, of course, have different chemical evolution histories than the Milky Way (e.g., Tolstoy et al. 2009; Hasselquist et al. 2021).

A comparison of the metallicity distribution function for this "single-star" control sample to that for the WD binary sample when limited to the most luminous objects ($M_H < -3.0$) shows clear differences (Figure 14), with the WD binary sample tending to be more metal-poor than the sample dominated by single stars. This may be a product of the strong anticorrelation between close binary fraction and chemical composition (Mazzola et al. 2020). The advantage of this comparison is that this metallicity difference is not driven by variations in sample volumes, since both the single-star and WD binary samples are drawn similarly from the same parent sample.

Meanwhile, at the low-luminosity end of the H-R diagram, there are a group of systems in Figure 13 outside of the selected areas in the CMD with temperatures lower than 4000 K. A careful look reveals that a few of them have large uncertainties in their parallaxes, making their distances, and hence their position in the CMD, less reliable. We checked these and confirmed that they are young stellar objects in known star-forming regions. However, the ones close to the MS binary sequence (Group 5) show very large values for the Gaia parameter Renormalized Unit Weight Error (RUWE), suggesting that they are multiple systems (e.g., Belokurov et al. 2020; Stassun & Torres 2021) potentially containing a WD.

Finally, we highlight the existence of what appears to be a prominent SSG population within the WD binary sample (represented by region 6 in Figure 13). SSG stars have been recognized as likely representing unusual stellar evolution pathways ever since their initial detection as anomalies in the CMDs of some open clusters (see, e.g., Mathieu et al. 2003, and references therein). Subsequent studies of SSGs in clusters have proffered several possible interpretations for these systems: mass transfer in a binary system, collision of two MS stars, mass loss of subgiant envelopes through dynamical encounters, and reduced luminosity due to the strong surface coverage of magnetic starspots (see, e.g., Leiner et al. 2017). Some recent works have concluded that mass transfer and

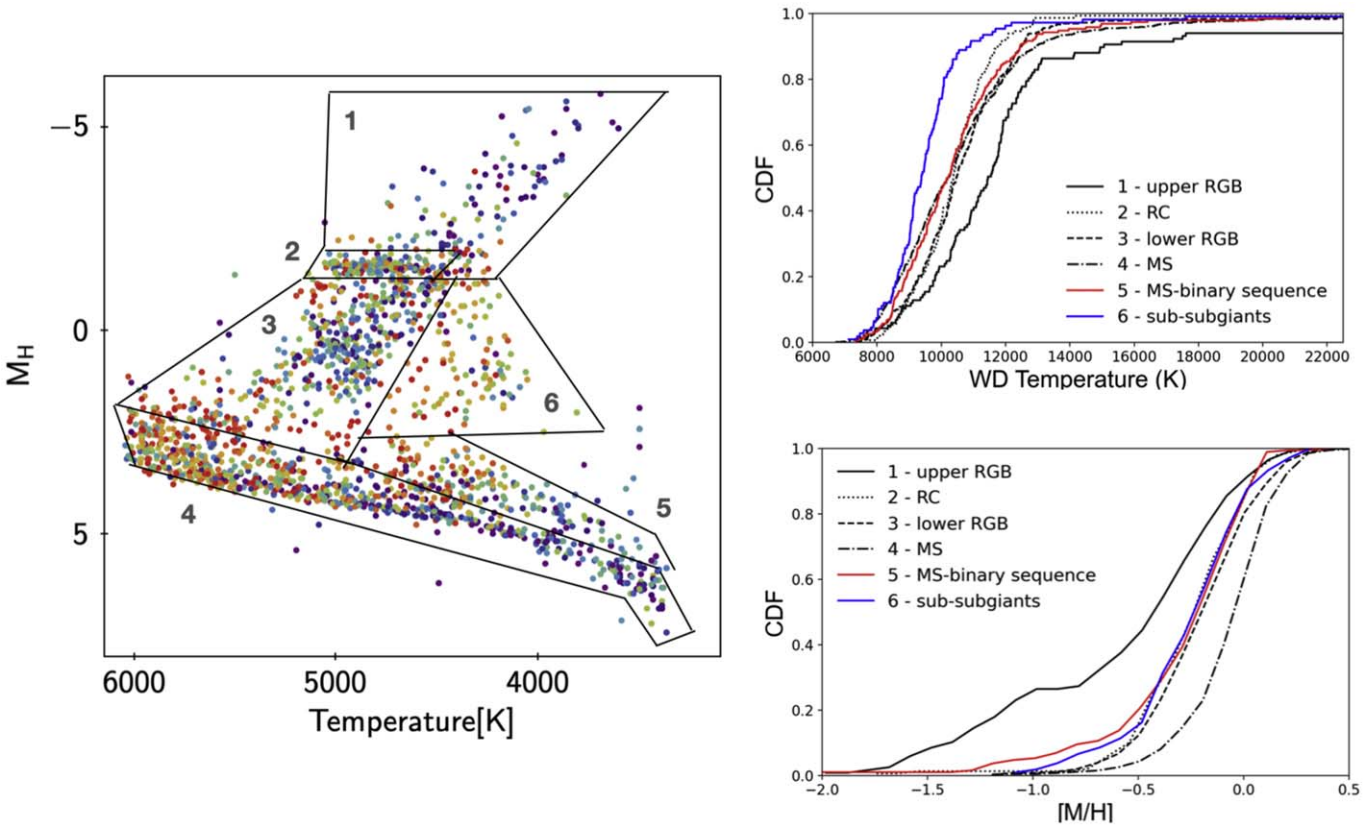

Figure 13. Left panel: same as Figure 12, but now divided into regions corresponding to principal stellar evolutionary phases: 1—upper RGB; 2—RC; 3—lower RGB; 4—MS; 5—MS binary sequence; and 6—SSGs. Right panel: the CDFs of both the WD temperature (top panel) and overall metallicity (bottom panel) for stars lying in the different regions of the CMD. The upper RGB shows a larger number of hotter WDs, and the metallicity distribution for these systems is clearly skewed to lower metallicities with respect to those in the other regions of the CMD, while the MS group of binary candidates shows the largest number of metal-rich objects.

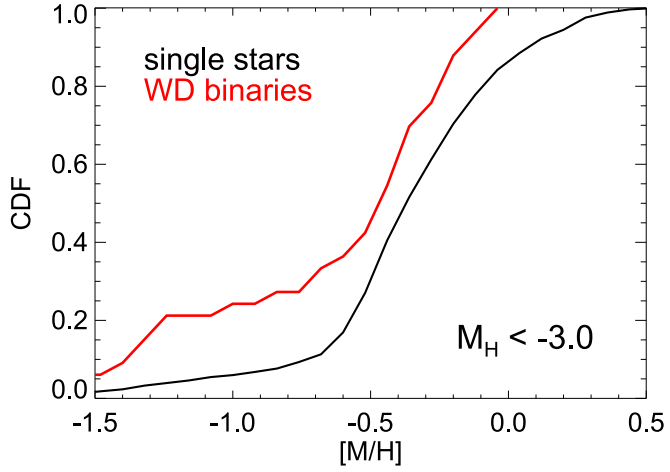

Figure 14. Overall metallicity from the APOGEE spectra CDF for objects with $M_H < -3.0$. The black line is for a sample dominated by single stars, and the red line is for the WD binary sample discussed in this work. For the most luminous stars the MDF is clearly different for the binary and nonbinary samples.

dynamical formation pathways are disfavored based on the small numbers of SSGs in open clusters, preferring instead the strong starspot interpretation (e.g., Gosnell et al. 2022). However, attempts to identify and characterize the broader SSG population in the field have only very recently begun (Leiner et al. 2022). Thus, the large population of apparent SSGs in the field identified in Figure 13, and in particular the knowledge in this work that these SSGs all possess a WD companion, could be an opportunity to make substantial new progress in understanding these enigmatic systems.

For example, one possibility for creating an SSG–WD system could be through a mass transfer channel. This could involve a scenario such as the following: First, start with an MS–MS binary in a wide orbit. When the more massive MS star evolves into a giant, unstable mass transfer occurs so that the system evolves through a CE. Given the temperature of the WDs we infer for these systems, the cooling ages suggest that this would have occurred on the order of a few hundred Myr ago. Following the CE phase, the system emerges as a MS–WD binary with an orbital period of a few days or less. Finally, the remaining MS star begins to evolve off the MS, and mass transfer starts again on the subgiant branch. As it loses mass, this second star evolves into the SSG region of the H-R diagram, as demonstrated by Leiner et al. (2017). The specific evolutionary track depends on the mass of the SSG, the mass of the WD, the initial orbital separation, and the fraction of the mass lost by the donor that is accreted by the companion. However, representative tracks from Leiner et al. (2017) are shown in Figure 15, and these suggest that at least some of the SSG+WD systems we have identified could plausibly represent such a scenario. Assuming different initial conditions, such as alternative subgiant star masses, could potentially shift the tracks in Figure 15 to cover more of the SSG+WD parameter space that we observe.

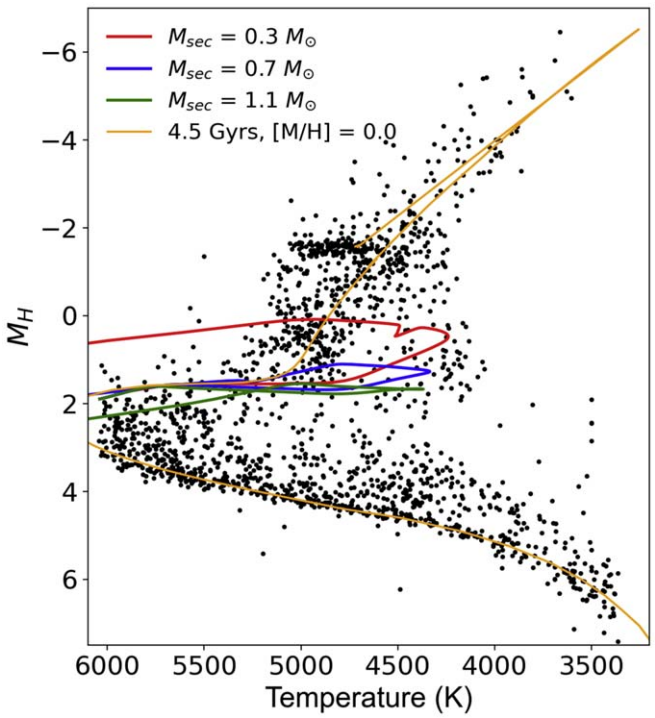

Figure 15. Exploring potential SSG systems in our catalog. Superposed are evolutionary models from Leiner et al. (2017) of SSGs experiencing mass transfer. All models assume a 1.3 $M_\odot$ subgiant primary with a compact companion in a 1.0-day orbit. Mass of the companion for each system is indicated by color of the track: 1.1 $M_\odot$ (green), 0.7 $M_\odot$ (blue), and 0.3 $M_\odot$ (red). The Leiner et al. (2017) models have been arbitrarily shifted 200 K cooler to better match the observed span of the SSG+WD candidate systems we observe, suggesting that similar evolutionary configurations but with different initial conditions (e.g., different subgiant mass, etc.) could potentially explain the diversity of SSG+WD systems we have identified. We also show in yellow a 4.5 Gyr solar-metallicity isochrone (Bressan et al. 2012)

Additional detailed modeling of these intriguing possibilities will be an exciting direction of exploration for a future analysis leveraging the catalog of WD binaries presented in this paper.

5.2. Binary Properties as a Function of RV Variability and Orbital Period

An advantage conferred by the APOGEE survey is that multi-epoch data were obtained, and RVs from these multiple epochs enable studies of stellar and substellar multiplicity (Troup et al. 2016; Badenes et al. 2018; Lewis et al. 2022).[15] When a sufficient number of epochs are available for a particular star, it is possible to derive or constrain orbital parameters (e.g., Price-Whelan et al. 2020; see below); however, this only applies to a minority fraction of APOGEE targets, since the more typical number of APOGEE visits is only three per star. However, under such circumstances it is still possible to undertake a statistical assessment of the number of stars with close companions, thereby accessing a majority of the APOGEE sample.

A particularly sensitive parameter for this purpose is the difference between the highest and lowest measured RVs for each WD binary candidate, $\Delta RV_{max} = max(RV) - min(RV)$ (see Badenes & Maoz 2012, for a discussion of this metric). Figure 16 shows the cumulative histograms for ΔRV_{max} in two samples: (1) the full APOGEE DR17 sample (blue solid line) following a similar selection to that described in Mazzola et al. (2020), and (2) the main WD binary sample (orange solid line). In this case, we divide the analysis into three broad categories, (a) the "cold MS" ($T_{eff} < 5500$ K and $\log g < 4.0$), (b) the RGB ($T_{eff} < 5500$ K and $\log g > 4.0$), and (c) the RC, using the catalog of RC stars in the APOGEE DR17 sample following Bovy et al. (2014). We show these divisions in the top left panel of Figure 16, where blue points show the APOGEE DR17 reference sample and orange points show the WD binary catalog. As may be seen in the other three panels of Figure 16, the ΔRV_{max} CDF for the WD binaries (orange solid lines) is clearly skewed toward larger ΔRV_{max} values, suggesting shorter periods for these systems. The RC sample shows the largest difference between the WD binary sample and the APOGEE reference sample. These results can be interpreted as evidence for drastic loss of angular momentum associated with the formation of the WD, most naturally explained by a CE episode leading to the ejection of at least some of the envelope of the mass primary/WD progenitor.

The above statistical analysis of orbital kinematics in the WD binary sample already unlocks tantalizing results worthy of further exploration. But the WD binary sample drawn from the AGGC has also produced the largest sample of such systems having uniformly derived orbital parameters. These systems, which contain secondaries broadly spanning the H-R diagram, are a uniquely powerful tool to be exploited for very detailed analyses of WD binary evolution. To explore this potential, we rely here on an APOGEE DR17 value-added catalog (Price-Whelan et al. 2020) containing posterior samplings of Keplerian orbital parameters (e.g., orbital period) derived using The Joker (Price-Whelan et al. 2017) for all DR17 stars having three or more APOGEE RV measurements. For this exercise, we select out a preliminary set of likely binaries, where we select RV-variable sources using a log likelihood ratio comparing The Joker's best fit of the APOGEE RVs to a best-fit constant-velocity model. Cross-matching our catalog with this value-added catalog yields 252 potential WD binaries having well-constrained orbital periods. More than half of the systems have more than four epochs, while around 120 systems have $3 \leqslant$ epochs $\leqslant 4$. Nearly all the systems show an uncertainty in their periods smaller than 1 day.

Figure 17 shows the H-R diagram of these 252 likely WD binaries having well-constrained orbital periods, with symbols color-coded by the derived orbital period in days. While the WD binary candidates cover widely the range of sensitivity for the combined, decade-long APOGEE-1 and APOGEE-2 surveys, a large fraction of our systems show periods of only a few days. The right panel of Figure 17 shows the CDF of the orbital period for the 252 sample stars, broken up similarly into the six secondary-star evolutionary groups used in Section 5.1 (compare the left panel of Figure 17 with the left panel of Figure 13). While the orbital period distributions show a similar behavior for the upper and lower RGB and the MS, the RC distribution appears to be heavily diminished in the number of short-period systems. This likely is the result of the clearing out of residual short-period systems during a second CE phase (Badenes et al. 2018). Meanwhile, the systems lying in the MS binary and SSG groups are heavily biased toward indicating the presence of a short-period system. In the case of the SSG group, the presence of a close binary is consistent with the

[15] The detection of stellar multiplicity as evidenced by RV variability was one of the motivations for APOGEE being a multi-epoch survey (Majewski et al. 2017).

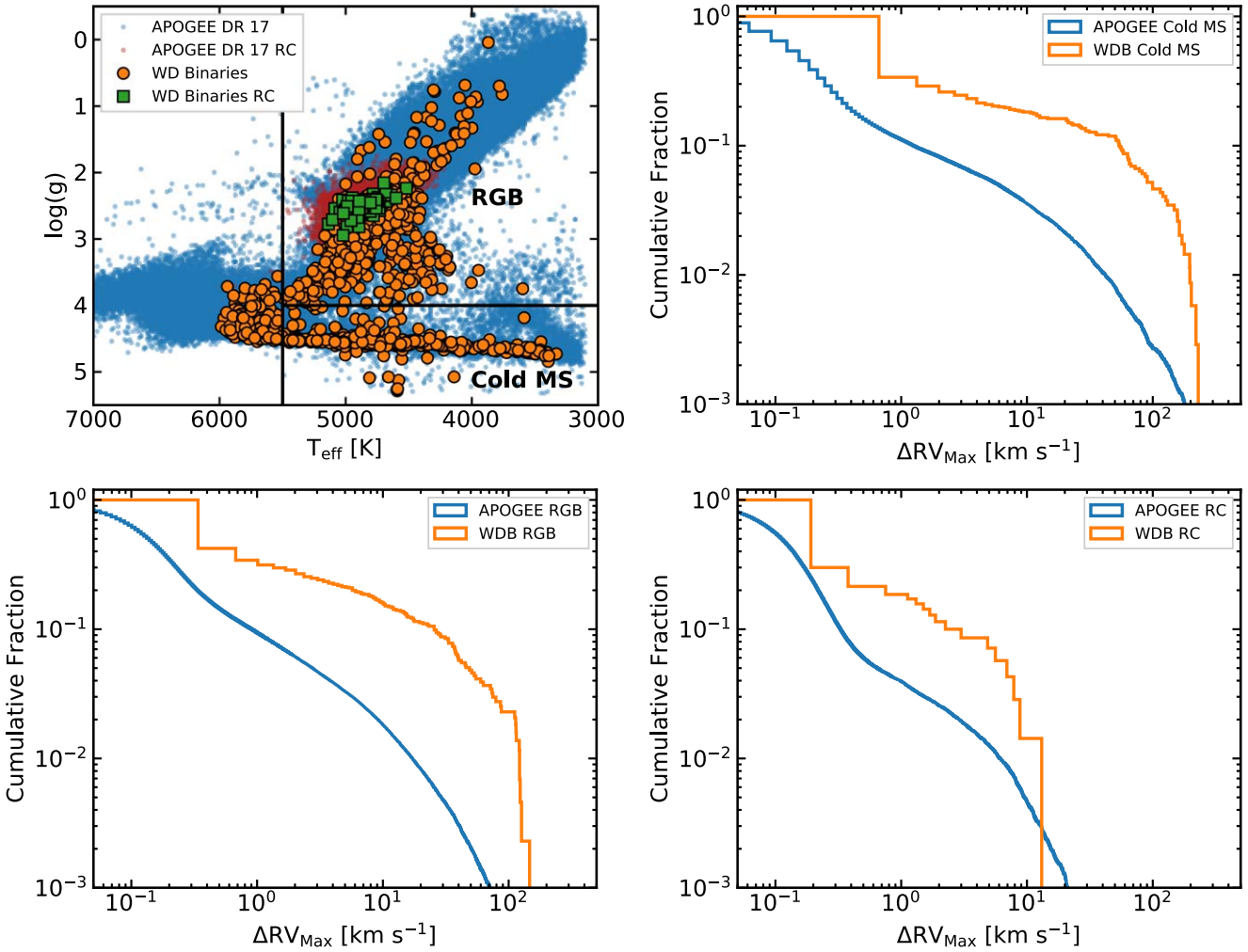

Figure 16. Top left panel: $T_{\rm eff}$–log g diagram for the APOGEE DR17 control sample (blue) and the WD binary catalog (orange). The selection of cold MS, RGB, and RC is also shown. Top right panel, bottom left and right panels: ΔRV_{max} cumulative fraction histogram for the cold MS sample, RGB, and RC in the APOGEE (blue) and WD binary catalogs (orange), respectively. The cumulative fraction for the WD binaries is skewed toward larger ΔRV_{max} with respect to the APOGEE control sample for the three selected populations.

subgiant–WD mass transfer formation channel discussed in Section 5.1 and featured in Figure 15. In the case of the MS binary group, which are putative triple systems including a WD, the skew toward short-period binaries seen in Figure 17 may reflect evolution of the hierarchical systems due to the Kozai–Lidov mechanism (Thompson 2011). However, these systems could also be binaries with low-mass WDs, where the systems are descended from short-period MS binaries (e.g., Lagos et al. 2022), since such systems are known to very frequently host a distant tertiary (Tokovinin et al. 2006). Moe & Kratter (2018) have pointed out that the occurrence rate of tertiaries to short-period binaries cannot be caused by the Kozai–Lidov mechanism alone.

WD binaries with orbital periods of $P < 100$ days are strong PCEB candidates. The cutoff at a 100-day orbital period should exclude most binaries that have had no stable mass transfer (Nebot Gómez-Morán et al. 2011; Kruckow et al. 2021). Recently, Lagos et al. (2022) suggested that PCEBs are only systems with periods below 5 days, while systems with periods of the order of several weeks to months could be the result of stable and nonconservative mass transfer. The evolution of PCEBs is driven by angular momentum loss due to gravitational radiation (Chernoff & Finn 1993) and disrupted magnetic braking (Verbunt & Zwaan 1981; Rappaport et al. 1983). Subsequent evolution may bring the system into a semidetached configuration. CVs, composed of a WD as the primary and a low-mass star or a brown dwarf as the secondary, belong to this type of semidetached system, where the secondary fills its critical lobe and transfers mass toward the primary (Warner 2003).

How the CE phase and the mass loss affect binary evolution and the chemical abundances measured for compact binaries is still not well understood (see, e.g., Mazzola et al. 2020, and references therein). Motivated by this problem, Figure 18 shows the metallicity as a function of the orbital period for the 252 WD binary candidates with well-established periods. As mentioned above (and illustrated in Figure 17), a large fraction of these systems show an orbital period of a few days, and this is in good agreement with the ΔRV_{max} exercise performed on the much larger sample of WD binaries having only a few epochs of data discussed even earlier, where the WD binaries clearly have larger ΔRV_{max} than the bulk of the DR17 stars. The results of both of these analyses suggest that their period distributions must be skewed toward shorter periods, presumably as a result of CE evolution. Using the CDF for three different samples selected using the orbital period, we find that

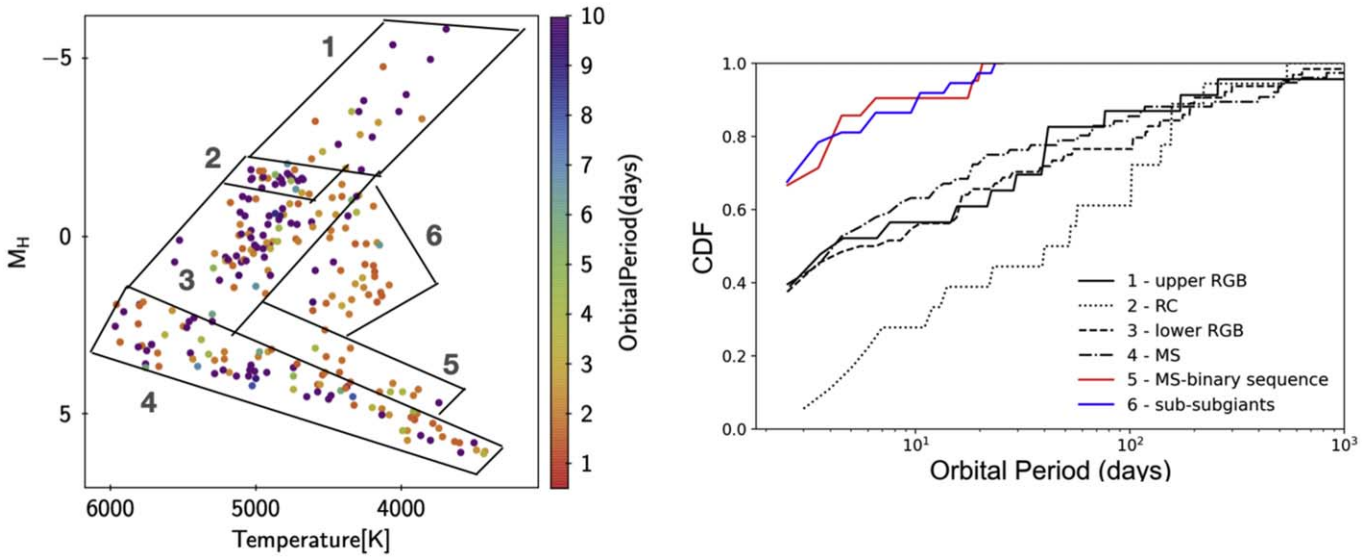

Figure 17. Left panel: the CMD distribution of WD binaries having reliable, full orbital fits to the APOGEE multi-epoch RVs, color-coded by the derived orbital period. We divide the sample of 252 such systems into secondary-star evolutionary stages as follows: 1—upper RGB; 2—RC; 3—lower RGB; 4—MS; 5 MS binary sequence; and 6—SSGs. Right panel: cumulative fraction of the orbital period in days for the different CMD groupings. The RC, the MS binary sequence, and the SSGs have clearly a different period distribution with respect to the other CMD groups. The RC systems show the smallest number of short-period binaries, while the MS binary sequence and the SSGs are greatly skewed to having the largest number of short-period binaries.

the sample dominated by wide binaries ("WB," defined here as $P > 100$ days) is skewed to lower metallicities than the sample dominated by PCEB candidates ($P < 100$ days). We also note that systems with $P < 5$ days show a similar metallicity distribution (red solid line in Figure 18); thus, at least in terms of metallicity distribution, there is no apparent difference with this more strict definition of the likely PCEB systems. The Figure 18 results are in agreement with our previous analysis of the metallicity distribution for 21 WDMS systems separated into their respective classifications as WB or PCE systems (Corcoran et al. 2021). Here we validate that previous, somewhat tentative result derived from a very small fraction of the AGGC-produced WD binary sample with the now much larger sample of WD binaries that more broadly cover the H-R diagram. Both studies therefore suggest that there is some sort of enrichment of the secondary star's surface chemistry during the CE phase.

As one final demonstration of the scientific reach of our new catalog of 3414 WD binary candidates, we identify within it some 54 metal-poor systems ([M/H] < -1.0), among them four with [M/H] < -2.0, and one system with [M/H] $= -2.4$, making it the most metal-poor WD binary candidate (Corcoran et al. 2021). Among the 252 systems having well-defined orbital solutions, Figure 18 shows orbital periods ranging from a few days to a few thousand days for eight systems having [M/H] < -1.0.

6. Conclusions

A majority of MS stars exist in binary systems (e.g., Jaschek & Gómez 1970; Duchêne & Kraus 2013; Price-Whelan et al. 2020, and references therein), with ∼70% of them predicted to interact with their companion(s) during their lifetime, even higher in the massive regime (Kobulnicky et al. 2014). It is not possible to develop a comprehensive theory of stellar evolution without taking into account stellar multiplicity (e.g., De Marco & Izzard 2017). In this study we focused on potential WD binaries found within the APOGEE survey using the AGGC (Section 2) and showed how the use of SEDs including UV-band photometry is an efficient method to identify such objects (e.g., Morgan et al. 2012; Parsons et al. 2016).

One of the least understood phases of compact binary evolution is the CE phase (Paczynski 1976), where one of the main issues is our ignorance of the efficiency of the energy transfer between the orbit and the envelope of the primary. Furthermore, we cannot predict the relationship between pre-CE and post-CE populations (Izzard et al. 2012; De Marco & Izzard 2017). The types of advances that can be expected from exploration of the AGGC are demonstrated by our analysis of 45 previously classified WDMS binaries (identified by SDSS and LAMOST) that have also been observed by APOGEE (Corcoran et al. 2021). Based on that pilot survey, Corcoran et al. (2021) show that the wide binary stars in the sample have a metallicity distribution function (MDF) that is significantly skewed to lower metallicities than the PCEB stars. That sample was mainly limited to WD–M-dwarf pairs. Here we extended the Corcoran et al. (2021) study to the much larger AGGC to characterize many more previously *unknown* WDMS systems, as well as systems with evolved secondaries.

A particular contribution here is the subcatalog containing 252 systems with well-constrained orbits from The Joker (Price-Whelan et al. 2017; see Section 5.2). For a larger sample than Corcoran et al. (2021) and across the H-R diagram, we find that a sample dominated by WB ($P > 100$ days) is skewed to lower metallicities than a sample dominated by PCEB stars ($P < 100$ days). Moreover, a detailed comparison between a sample dominated by WD binaries and other samples containing mainly single stars (see Section 5.1) shows that there is a prominent difference between the MDFs for the most luminous giants, $M_H < -3.0$ (see Figure 14). This range of absolute magnitude might contain a large fraction of RG and AGB stars, where the stellar radii can reach sizes of several astronomical units. Binary interactions can have an impact on the intrinsic properties of an evolved star: it can alter the pulsations, the mass-loss efficiency and geometry, the dust formation processes, and the circumstellar envelope morphology. Binary

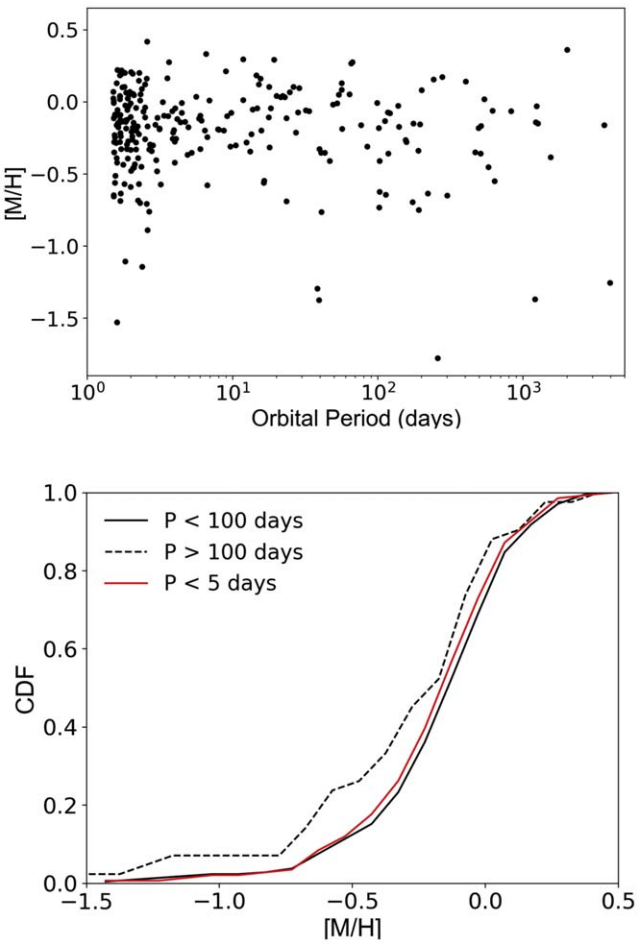

Figure 18. Top panel: period–metallicity distribution for the 252 WD binaries in our sample with well-defined orbital solutions fit to the APOGEE RVs. The vast majority of these binaries have an orbital period of a few days but span a wide metallicity range ($-0.7 < [M/H] < +0.3$). A number of metal-poor ([M/H] < -1) systems are found covering a broad range of periods. Bottom panel: the CDF of the metallicity for three samples selected according to the orbital period. The solid black line represents systems with $P < 100$ days and the red solid line systems with $P < 5$ days, while the dashed line shows binaries where $P > 100$ days. Systems with shorter orbital periods tend to have higher metallicity.

interaction can even play a dominant role in determining the ultimate fate of the object, i.e., the formation of CVs, SNe Ia, barium stars, gravitational-wave sources, etc. (Jones & Boffin 2017; Oomen et al. 2018). Our findings support the scenario where there is an enrichment of a system's surface chemistry during the CE phase. While in this pilot study we only explored the overall metallicity measured from the APOGEE spectra, in future work we will study in detail the abundance differences in the WD binary sample created here for other, individual chemical elements (the abundances of more than 15 elements exist in the APOGEE catalog, including C, N, O, Na, Mg, Al, Si, S, K, Ca, Ti, V, Mn, Fe, and Ni).

7. Summary

In this paper we present a systematic search for compact binary star systems containing WDs, created by harnessing information contained in the spectroscopic catalog of the APOGEE project (Majewski et al. 2017), matched with the data from the Gaia (Lindegren et al. 2018) and GALEX (Bianchi et al. 2017) space missions. The results of our investigation of these systems are as follows:

1. We have created (Section 2) the AGGC. Systems with $T_{\rm eff} < 6000$ K and $(\mathrm{FUV-NUV})_o < 5$ are the most compelling for our purposes. Based on these selections, we have identified 3414 APOGEE sources that are potential WD binary candidates having F–M spectral type companions.
2. We use the empirical SED from the UV to the IR for the AGGC sample to derive system parameters like the WD temperature and radius (Section 3). The radius diagram (Section 4, Figure 10) provides a useful criterion for creating a relatively clean sample of WD binary candidates within the AGGC sample, where a total of 1806 stars have WD radii that fall below 25 $R_\oplus$ and constitute a more reliable sample of WD binary candidates.
3. The most luminous ($M_H < -3.0$) secondaries in our WD binary candidate sample clearly show a different MDF with respect to a control sample dominated by single stars of similar luminosity (Section 5.1, Figure 14). This may have to do with the effects of binary companions on the chemical evolution of the AGB population—e.g., in how many are converted into carbon stars. We have previously shown how symbiotic stars identified in our catalog show enhancement in carbon abundance (e.g., Lewis et al. 2020; Washington et al. 2021).
4. We also highlight (Section 5.1) the existence of an SSG population (e.g., Belloni et al. 1998; Mathieu et al. 2003) in Figures 12 and 13. These objects are X-ray sources and photometric variables. Where binary status is known, they are often found to be close binary systems with orbital periods on the order of 1–10 days (Leiner et al. 2017; Geller et al. 2017). In this exercise we found that the orbital period associated with these objects ranges from a few days to ∼20 days (see Figure 13), in agreement with the literature. The SSGs in this sample potentially contain a WD companion; this sample could be an opportunity to make substantial new progress in understanding these intriguing systems with additional detailed modeling.
5. The $\Delta \mathrm{RV}_{\rm max}$ cumulative fraction for the WD binaries is skewed toward larger $\Delta \mathrm{RV}_{\rm max}$ values with respect to the APOGEE DR17 control sample (Section 5.2, Figure 16). This result suggests shorter periods for these systems and evidence for drastic loss of angular momentum associated with the formation of the WD. We also investigated 252 potential WD binaries with estimated orbital periods. From these we find a large fraction to show an orbital period of a few days, typical of binary systems whose orbits have circularized (Figure 17). From the CDF of two different samples selected using the orbital period, we found (Figure 18) that the sample dominated by wide binaries ($P > 100$ days) is skewed to lower metallicities than the sample dominated by PCEB stars ($P < 100$ days). This finding suggests an enrichment of a system's surface chemistry during the CE phase.

The AGGC is a rich resource for investigating the evolution of WD binaries across the H-R diagram. Here we have only touched various avenues that are ripe for further development. Among the additional available tools that we intend to exploit

in our future efforts are the more than 15 elements derived in the APOGEE catalog for the WD binary sample, and looking more deeply into the orbital properties of the systems, beyond simple periods.

We thank the referee for comments that helped improve this paper. B.A. acknowledges support from a Chrétien International Research Grant from the American Astronomical Society. B.A. and S.R.M. acknowledge support from National Science Foundation grant AST-1616636. The authors acknowledge helpful discussions with E. Leiner regarding SSGs and for sharing SSG evolution models. Funding for the Sloan Digital Sky Survey IV has been provided by the Alfred P. Sloan Foundation, the U.S. Department of Energy Office of Science, and the Participating Institutions. SDSS-IV acknowledges support and resources from the Center for High-Performance Computing at the University of Utah. The SDSS website is www.sdss.org. SDSS is managed by the Astrophysical Research Consortium for the Participating Institutions of the SDSS Collaboration, including the Brazilian Participation Group, the Carnegie Institution for Science, Carnegie Mellon University, the Chilean Participation Group, the French Participation Group, Harvard-Smithsonian Center for Astrophysics, Instituto de Astrofísica de Canarias, Johns Hopkins University, Kavli Institute for the Physics and Mathematics of the Universe (IPMU)/University of Tokyo, the Korean Participation Group, Lawrence Berkeley National Laboratory, Leibniz Institut für Astrophysik Potsdam (AIP), Max-Planck-Institut für Astronomie (MPIA Heidelberg), Max-Planck-Institut für Astrophysik (MPA Garching), Max-Planck-Institut für Extraterrestrische Physik (MPE), National Astronomical Observatories of China, New Mexico State University, New York University, University of Notre Dame, Observatório Nacional/MCTI, The Ohio State University, Pennsylvania State University, Shanghai Astronomical Observatory, United Kingdom Participation Group, Universidad Nacional Autónoma de México, University of Arizona, University of Colorado Boulder, University of Oxford, University of Portsmouth, University of Utah, University of Virginia, University of Washington, University of Wisconsin, Vanderbilt University, and Yale University. This research has made use of the SIMBAD database, operated at CDS, Strasbourg, France. This publication makes use of VOSA, developed under the Spanish Virtual Observatory project supported by the Spanish MINECO through grant AyA2017-84089. VOSA has been partially updated by using funding from the European Union's Horizon 2020 Research and Innovation Programme, under grant Agreement No 776403 (EXOPLANETS-A). This research has made use of NASA's Astrophysics Data System Bibliographic Services (NASA ADS). This research made use of Astropy,[16] a community-developed core Python package for Astronomy.

ORCID iDs

Borja Anguiano https://orcid.org/0000-0001-5261-4336
Steven R. Majewski https://orcid.org/0000-0003-2025-3147
Keivan G. Stassun https://orcid.org/0000-0002-3481-9052
Carles Badenes https://orcid.org/0000-0003-3494-343X
Carlos Allende Prieto https://orcid.org/0000-0002-0084-572X
Donald P. Schneider https://orcid.org/0000-0001-7240-7449
Adrian M. Price-Whelan https://orcid.org/0000-0003-0872-7098
Rachael L. Beaton https://orcid.org/0000-0002-1691-8217

[16] http://www.astropy.org

References

Abdurro'uf, Accetta, K., Aerts, C., et al. 2022, ApJS, 259, 35
Alekseev, I. Y. 2000, ARep, 44, 696
Amado, P. J., & Byrne, P. B. 1997, A&A, 319, 967
Anguiano, B., Lewis, H. M., Corcoran, K. A., et al. 2020, RNAAS, 4, 127
Anguiano, B., Rebassa-Mansergas, A., García-Berro, E., et al. 2017, MNRAS, 469, 2102
Badenes, C., & Maoz, D. 2012, ApJL, 749, L11
Badenes, C., Mazzola, C., Thompson, T. A., et al. 2018, ApJ, 854, 147
Bailer-Jones, C. A. L., Rybizki, J., Fouesneau, M., et al. 2021, AJ, 161, 147
Baliunas, S. L., Donahue, R. A., Soon, W. H., et al. 1995, ApJ, 438, 269
Bayo, A., Rodrigo, C., Barrado Y Navascués, D., et al. 2008, A&A, 492, 277
Beaton, R. L., Oelkers, R. J., Hayes, C. R., et al. 2021, AJ, 162, 302
Belloni, T., Verbunt, F., & Mathieu, R. D. 1998, A&A, 339, 431
Belokurov, V., Penoyre, Z., Oh, S., et al. 2020, MNRAS, 496, 1922
Bergeron, P., Wesemael, F., & Beauchamp, A. 1995, PASP, 107, 1047
Bianchi, L., Efremova, B., Herald, J., et al. 2011, MNRAS, 411, 2770
Bianchi, L., Shiao, B., & Thilker, D. 2017, ApJS, 230, 24
Biazzo, K., Frasca, A., Catalano, S., et al. 2006, A&A, 446, 1129
Blanton, M. R., Bershady, M. A., Abolfathi, B., et al. 2017, AJ, 154, 28
Bleach, J. N., Wood, J. H., Smalley, B., et al. 2002, MNRAS, 335, 593
Bopp, B. W., & Fekel, F. 1977, AJ, 82, 490
Boro Saikia, S., Marvin, C. J., Jeffers, S. V., et al. 2018, A&A, 616, A108
Bovy, J., Nidever, D. L., Rix, H.-W., et al. 2014, ApJ, 790, 127
Bowen, I. S., & Vaughan, A. H. 1973, ApOpt, 12, 1430
Bressan, A., Marigo, P., Girardi, L., et al. 2012, MNRAS, 427, 127
Castelli, F., Gratton, R. G., & Kurucz, R. L. 1997, A&A, 318, 841
Chernoff, D. F., & Finn, L. S. 1993, ApJL, 411, L5
Clementini, G., Ripepi, V., Molinaro, R., et al. 2019, A&A, 622, A60
Corcoran, K. A., Lewis, H. M., Anguiano, B., et al. 2021, AJ, 161, 143
Da Costa, A. D., Canto Martins, B. L., Leão, I. C., et al. 2017, ApJ, 837, 15
De Marco, O., & Izzard, R. G. 2017, PASA, 34, e001
Duchêne, G., & Kraus, A. 2013, ARA&A, 51, 269
Eisenstein, D. J., Liebert, J., Harris, H. C., et al. 2006, ApJS, 167, 40
Eker, Z., Ak, N. F., Bilir, S., et al. 2008, MNRAS, 389, 1722
Fitzpatrick, E. L. 1999, PASP, 111, 63
García Pérez, A. E., Allende Prieto, C., Holtzman, J. A., et al. 2016, AJ, 151, 144
Geller, A. M., Leiner, E. M., Bellini, A., et al. 2017, ApJ, 840, 66
Gosnell, N. M., Gully-Santiago, M. A., Leiner, E. M., et al. 2022, ApJ, 925, 5
Gunn, J. E., Siegmund, W. A., Mannery, E. J., et al. 2006, AJ, 131, 2332
Hasselquist, S., Hayes, C. R., Lian, J., et al. 2021, ApJ, 923, 172
Heller, R., Homeier, D., Dreizler, S., et al. 2009, A&A, 496, 191
Hernandez, M. S., Schreiber, M. R., Parsons, S. G., et al. 2021, MNRAS, 501, 1677
Hjellming, M. S., & Taam, R. E. 1991, ApJ, 370, 709
Holtzman, J. A., Hasselquist, S., Shetrone, M., et al. 2018, AJ, 156, 125
Idan, I., Lasota, J.-P., Hameury, J.-M., et al. 2010, A&A, 519, A117
Ivanova, N., Justham, S., Chen, X., et al. 2013, A&ARv, 21, 59
Izzard, R. G., Hall, P. D., Tauris, T. M., et al. 2012, IAU Symp. 283, Planetary Nebulae: An Eye to the Future (Cambridge: Cambridge Univ. Press), 95
Jaschek, C., & Gómez, A. E. 1970, PASP, 82, 809
Jones, D., & Boffin, H. M. J. 2017, NatAs, 1, 0117
Jones, D. O., & West, A. A. 2016, ApJ, 817, 1
Kepler, S. O., Pelisoli, I., Koester, D., et al. 2016, MNRAS, 455, 3413
Kinman, T. D., & Brown, W. R. 2014, AJ, 148, 121
Kobulnicky, H. A., Kiminki, D. C., Lundquist, M. J., et al. 2014, ApJS, 213, 34
Koester, D. 2010, Mem. Soc. Astron. Italiana, 81, 921
Kounkel, M., Covey, K., Suárez, G., et al. 2018, AJ, 156, 84
Kounkel, M., Covey, K. R., Stassun, K. G., et al. 2021, AJ, 162, 184
Kruckow, M. U., Neunteufel, P. G., Di Stefano, R., et al. 2021, ApJ, 920, 86
Lagos, F., Schreiber, M. R., Parsons, S. G., et al. 2022, MNRAS, 512, 2625
Leiner, E., Mathieu, R. D., & Geller, A. M. 2017, ApJ, 840, 67
Leiner, E. M., Geller, A. M., Gully-Santiago, M. A., et al. 2022, ApJ, 927, 222
Lewis, H. M., Anguiano, B., Majewski, S. R., et al. 2022, MNRAS, 509, 3355

Lewis, H. M., Anguiano, B., Stassun, K. G., et al. 2020, ApJL, 900, L43
Lindegren, L., Hernández, J., Bombrun, A., et al. 2018, A&A, 616, A2
Lindegren, L., Klioner, S. A., Hernández, J., et al. 2020, arXiv:2012.03380
Majewski, S. R., Schiavon, R. P., Frinchaboy, P. M., et al. 2017, AJ, 154, 94
Martínez-Arnáiz, R., Maldonado, J., Montes, D., et al. 2010, A&A, 520, A79
Mathieu, R. D., Adams, F. C., & Latham, D. W. 1991, AJ, 101, 2184
Mathieu, R. D., van den Berg, M., Torres, G., et al. 2003, AJ, 125, 246
Maxted, P. F. L., Gänsicke, B. T., Burleigh, M. R., et al. 2009, MNRAS, 400, 2012
Mazzola, C. N., Badenes, C., Moe, M., et al. 2020, MNRAS, 499, 1607
Merc, J., Gális, R., & Wolf, M. 2019, RNAAS, 3, 28
Mitnyan, T., Szalai, T., Bódi, A., et al. 2020, A&A, 635, A89
Moe, M., & Kratter, K. M. 2018, ApJ, 854, 44
Moe, M., Kratter, K. M., & Badenes, C. 2019, ApJ, 875, 61
Morgan, D. P., West, A. A., Garcés, A., et al. 2012, AJ, 144, 93
Nebot Gómez-Morán, A., Gänsicke, B. T., Schreiber, M. R., et al. 2011, A&A, 536, A43
Nebot Gómez-Morán, A., Schwope, A. D., Schreiber, M. R., et al. 2009, A&A, 495, 561
Nidever, D. L., Holtzman, J. A., Allende Prieto, C., et al. 2015, AJ, 150, 173
Oomen, G.-M., Van Winckel, H., Pols, O., et al. 2018, A&A, 620, A85
Paczynski, B. 1976, in IAU Symp. 73, Structure and Evolution of Close Binary Systems, ed. P. Eggleton, S. Mitton, & J. Whelan (Dordrecht: Reidel), 75
Parsons, S. G., Rebassa-Mansergas, A., Schreiber, M. R., et al. 2016, MNRAS, 463, 2125
Price-Whelan, A. M., Hogg, D. W., Foreman-Mackey, D., et al. 2017, ApJ, 837, 20
Price-Whelan, A. M., Hogg, D. W., Rix, H.-W., et al. 2020, ApJ, 895, 2
Provencal, J. L., Shipman, H. L., Høg, E., et al. 1998, ApJ, 494, 759
Queiroz, A. B. A., Anders, F., Chiappini, C., et al. 2020, A&A, 638, A76
Rappaport, S., Verbunt, F., & Joss, P. C. 1983, ApJ, 275, 713
Rebassa-Mansergas, A., Nebot Gómez-Morán, A., Schreiber, M. R., et al. 2012, MNRAS, 419, 806
Ren, J.-J., Rebassa-Mansergas, A., Parsons, S. G., et al. 2018, MNRAS, 477, 4641
Riello, M., De Angeli, F., Evans, D. W., et al. 2020, arXiv:2012.01916
Santana, F. A., Beaton, R. L., Covey, K. R., et al. 2021, AJ, 162, 303
Santiago, B. X., Brauer, D. E., Anders, F., et al. 2016, A&A, 585, A42
Schlegel, D. J., Finkbeiner, D. P., & Davis, M. 1998, ApJ, 500, 525
Schreiber, M. R., Gänsicke, B. T., Rebassa-Mansergas, A., et al. 2010, A&A, 513, L7
Schreiber, M. R., Gänsicke, B. T., Southworth, J., et al. 2008, A&A, 484, 441
Shipman, H. L. 1979, ApJ, 228, 240
Silvestri, N. M., Hawley, S. L., West, A. A., et al. 2006, AJ, 131, 1674
Skrutskie, M. F., Cutri, R. M., Stiening, R., et al. 2006, AJ, 131, 1163
Smith, G. H. 2018, PASA, 35, 37
Sokoloski, J. L., Kenyon, S. J., Espey, B. R., et al. 2006, ApJ, 636, 1002
Stassun, K. G., & Torres, G. 2016, AJ, 152, 180
Stassun, K. G., & Torres, G. 2021, ApJL, 907, L33
Steinmetz, M., Matijevič, G., Enke, H., et al. 2020, AJ, 160, 82
Stelzer, B., Marino, A., Micela, G., et al. 2013, MNRAS, 431, 2063
Tapia, M., Roth, M., & Persi, P. 2015, MNRAS, 446, 4088
Thompson, T. A. 2011, ApJ, 741, 82
Tokovinin, A., Thomas, S., Sterzik, M., et al. 2006, A&A, 450, 681
Toloza, O., Breedt, E., De Martino, D., et al. 2019, BAAS, 51, 168
Tolstoy, E., Hill, V., & Tosi, M. 2009, ARA&A, 47, 371
Tremblay, P.-E., Ludwig, H.-G., Steffen, M., et al. 2013, A&A, 559, A104
Troup, N. W., Nidever, D. L., De Lee, N., et al. 2016, AJ, 151, 85
Vaccaro, T. R., Wilson, R. E., Van Hamme, W., et al. 2015, ApJ, 810, 157
Verbunt, F., & Zwaan, C. 1981, A&A, 100, L7
Warner, B. 2003, in Cataclysmic Variable Stars, ed. B Warner (Cambridge: Cambridge Univ. Press), 592
Washington, J. E., Lewis, H. M., Anguiano, B., et al. 2021, ApJ, 918, 19
Webbink, R. F. 2008, in Short-Period Binary Stars: Observations, Analyses, and Results, Astrophysics and Space Science Library, Vol. 352, ed. E. F. Milone, D. A. Leahy, & D. W. Hobill (Berlin: Springer), 233
Welsh, B. Y., Wheatley, J. M., Heafield, K., et al. 2005, AJ, 130, 825
Wenger, M., Ochsenbein, F., Egret, D., et al. 2000, A&AS, 143, 9
Willems, B., & Kolb, U. 2004, A&A, 419, 1057
Wilson, J. C., Hearty, F. R., Skrutskie, M. F., et al. 2019, PASP, 131, 055001
Wright, E. L., Eisenhardt, P. R. M., Mainzer, A. K., et al. 2010, AJ, 140, 1868
York, D. G., Adelman, J., Anderson, J. E., et al. 2000, AJ, 120, 1579
Zasowski, G., Cohen, R. E., Chojnowski, S. D., et al. 2017, AJ, 154, 198
Zhao, G., Zhao, Y.-H., Chu, Y.-Q., et al. 2012, RAA, 12, 723